

Dome structures in collision orogens: Mechanical investigation of the gravity/compression interplay

Jean-Pierre Burg*
Boris J.P. Kaus
Yuri Yu. Podladchikov

Geologisches Institut, ETH and University Zürich, Sonneggstrasse 5, 8092 Zürich, Switzerland

ABSTRACT

Domes and basins are evidence for vertical movements in both compression and extension tectonic environments. They are thus evidence for interplay between gravity and tectonic forces in structuring the continental crust. We employ analytical and numerical techniques to investigate the respective roles of gravity and compression during the growth of crustal-scale buckle anticlines and diapirs submitted to instantaneous erosion. The analytical perturbation method, which explores the onset of both types of instability, yields a “phase-diagram” discriminating eight folding-diapirism modes, five of which are geologically relevant. Numerical simulations show that the phase diagram is applicable to evolved, finite amplitude stages. Calculated strain fields in both diapirs and folds show normal sense of shear at the interface if the upper layer is thick compared to the lower layer. We conclude that the present-day structural techniques applied for distinguishing diapiric domes and folds are ambiguous if detachment folding and intense erosion take place during deformation, and that domes displaying extensional structures do not necessarily reflect extension.

Keywords: doming, folding, diapirism, numerical modeling.

INTRODUCTION

Collision mountain systems are long, linear to arcuate belts at Earth’s surface. In these mountains, abundant folds and thrusts reflect regional shortening. Isostatic considerations, gravimetric studies, and seismic information show that horizontal shortening is intrinsically related to crustal thickening, and it requires 5–7 km of crustal root to balance each km of mountain range above sea level. In other words, a mountain grows 5–7 times more downward than upward. Consequently, collision-mountains are sites where the continental crust is buried, and thus subjected to intense metamorphism and igneous activity. Thickening of the buoyant crust and subsequent uplift create a high topography. The mountain belt also becomes a region of erosion, which digs out deep crustal levels and supplies sedimentary basins. The

long-term process results in ancient orogens being leveled to flatlands that expose metamorphic and magmatic rock associations, those that were part of the mountain roots. Typically, these high-grade metamorphic regions display large, closed structures termed domes and basins. Application of plate tectonics to understanding collision orogens has focused on horizontal movements because convergence is one to two orders of magnitude larger than orogenic vertical movements. Horizontal transport is classically inferred from recumbent folds and thrust systems. Domes and basins are evidence for vertical movements (e.g., Brun, 1983). Five distinct origins have been postulated:

- Folding: Many domes may be double plunging anticlines and/or culminations of crossing anticlines of two separate generations and different trends (Ramsay, 1967; Snowden and Bickle, 1976).

*jpb@erdw.ethz.ch

Burg, J.-P., Kaus, B.J.P., and Podladchikov, Y.Y., 2004, Dome structures in collision orogens: Mechanical investigation of the gravity/compression interplay, in Whitney, D.L., Teyssier, C., and Siddoway, C.S., Gneiss domes in orogeny: Boulder, Colorado, Geological Society of America Special Paper 380, p. 47–66. For permission to copy, contact editing@geosociety.org. © 2004 Geological Society of America

- Diapirism of igneous intrusions: A usual explanation of blob-like geological map patterns in high-grade metamorphic terranes postulates that mobilized rock masses rose buoyantly in the core of domes in response to the gravity instability resulting from the low density and viscosity of the granitic core below the denser and stronger wall rocks (e.g., Ramberg, 1972; Brun et al., 1981; Ramberg, 1981; Ramsay, 1989). This mechanism has been modeled mathematically (Fletcher, 1972; Ramberg, 1972) and experimentally (e.g., Dixon, 1975).
- Reactivation of basement plutons: The development of the type mantle gneiss domes in Finland (Eskola, 1949) invokes two orogenic events. During the first orogeny, granite plutons were emplaced in metasediments and metavolcanites. Erosion exposed the plutons and country rock, which were covered by a younger sequence of sediments. Injection of new magma during the second orogeny reactivated the old plutons, causing them to expand upward and thereby fold the overlying strata into domes and basins. We consider this interpretation as a restrictive case of polyorogenic yet superposed diapirism and/or folding.
- Extensional culminations: rocks of mid-crustal levels are brought to shallower levels by tectonic denudation and erosion, with horizontal extension along major, shallow-dipping detachments, scraping away the overlying cover (e.g., Coney and Harms, 1984).
- Upward impingement: A strong or rigid basement block forces bending of its plastic cover (Gzovsky et al., 1973).

These five mechanisms are not mutually exclusive. For example, fold interference is not incompatible with gravity instability since both mechanisms could operate synchronously, in particular where density contrast is invariably present between core and surrounding rocks (Snowden and Snowden, 1981). These five mechanisms produce upward movement of lower and mid-crustal levels during orogeny, but refer to different force systems since compression and extension are predominantly horizontal forces of opposite sign, and diapirism versus impingement involve predominantly vertical forces acting with and against gravity, respectively. By chance for geologists, they develop symptomatic structural features that allow for identification of which mechanism was dominant (Brun, 1983). In particular, extensional core complexes display a marked asymmetry of metamorphic grade and ages, contrasting with the symmetry in folds and diapirs (Fig. 1). Our aim is to discuss the growth and the mechanical characteristics of two types of domes in the light of two-dimensional numerical codes developed for the Ph.D. thesis of one of us (Kaus, 2004): (1) large upright folds for which upward amplification is fundamentally a response to horizontal compression, and (2) magmatic bodies for which diapiric (i.e., piercing) rise controlled by the vertical gravity seems to play a significant role. Extensional metamorphic core complexes in which rocks of middle crustal levels are uplifted and exposed by a process dominated by large offsets along low-

angle normal faulting are not discussed in this work; mechanical insight has been recently given by Lavier and Buck (2002).

CRUSTAL-SCALE FOLDS

Geological Information

Although geologists have demonstrated and accepted the existence of large recumbent folds (fold nappes) with some tens of kilometers-long inverted limbs (e.g., Arthaud, 1970; Ramsay, 1981), they resisted the concept of big buckle folds, with the intuitive belief that high amplitude, upright buckles could not stand against gravity (e.g., Ramberg, 1971). However, the concept becomes valid in places where erosion can behead crustal-scale anticlines during their growth, thus eliminating the height and relief problem. This is apparently the case in the Himalayan syntaxes for which the mechanical consistency of the erosion condition has been tested numerically (Burg and Podladchikov, 1999, 2000). In these Himalayan regions, buckle folding has allowed exhumation of 30-km-deep rocks within the last 5 m.y. (Zeitler et al., 1993; Burg et al., 1997; Burg et al., 1998). Such neotectonic examples bring support to crustal fold interpretation of older domes such as in the Variscides (Stipska et al., 2000) and some mantled gneiss domes (Snowden and Bickle, 1976), although the folding perception has gone out of fashion. The apparent lack of periodically spaced anticlines neighboring domes interpreted as folds is a common criticism of the buckle interpretation since smaller scale simulations emphasize periodicity in buckling (e.g., Currie et al., 1962; Smith, 1977). The relative isolation of large-scale folds is a puzzling singularity on which we will comment in the light of the numerical modeling presented here.

Mechanical Background

A considerable body of work has shown, both theoretically and experimentally, that if a thin layer undergoing layer-parallel shortening is more competent (i.e., stiffer) than the surrounding material, this condition is unstable and buckling as an instability of the stiff layer will occur, while the entire system is deforming in pure shear (e.g., Price and Cosgrove, 1990). Early work focused on the analysis of buckling of a layer, either elastic or viscous, in an infinite viscous matrix, taking into account a simple linear relationship between stress and strain or stress and strain-rate (Smoluchowski, 1910; Biot, 1961; Ramberg, 1964; Ramberg and Stephansson, 1964). Modeling relevant to lithospheric-scale deformation assumes that a power law viscous layer of thickness H (representing the crust) floats on a viscous halfspace (representing the mantle; Fig. 2A). We used a setup similar to that of Schmalholz et al. (2002), and we additionally implemented rapid erosion at the top surface and considered an inverse density contrast between the layer and the underlying halfspace. If the viscous lower halfspace does not exert any shear stress on the layer, the thin-plate theory applies (e.g., Reddy, 1999).

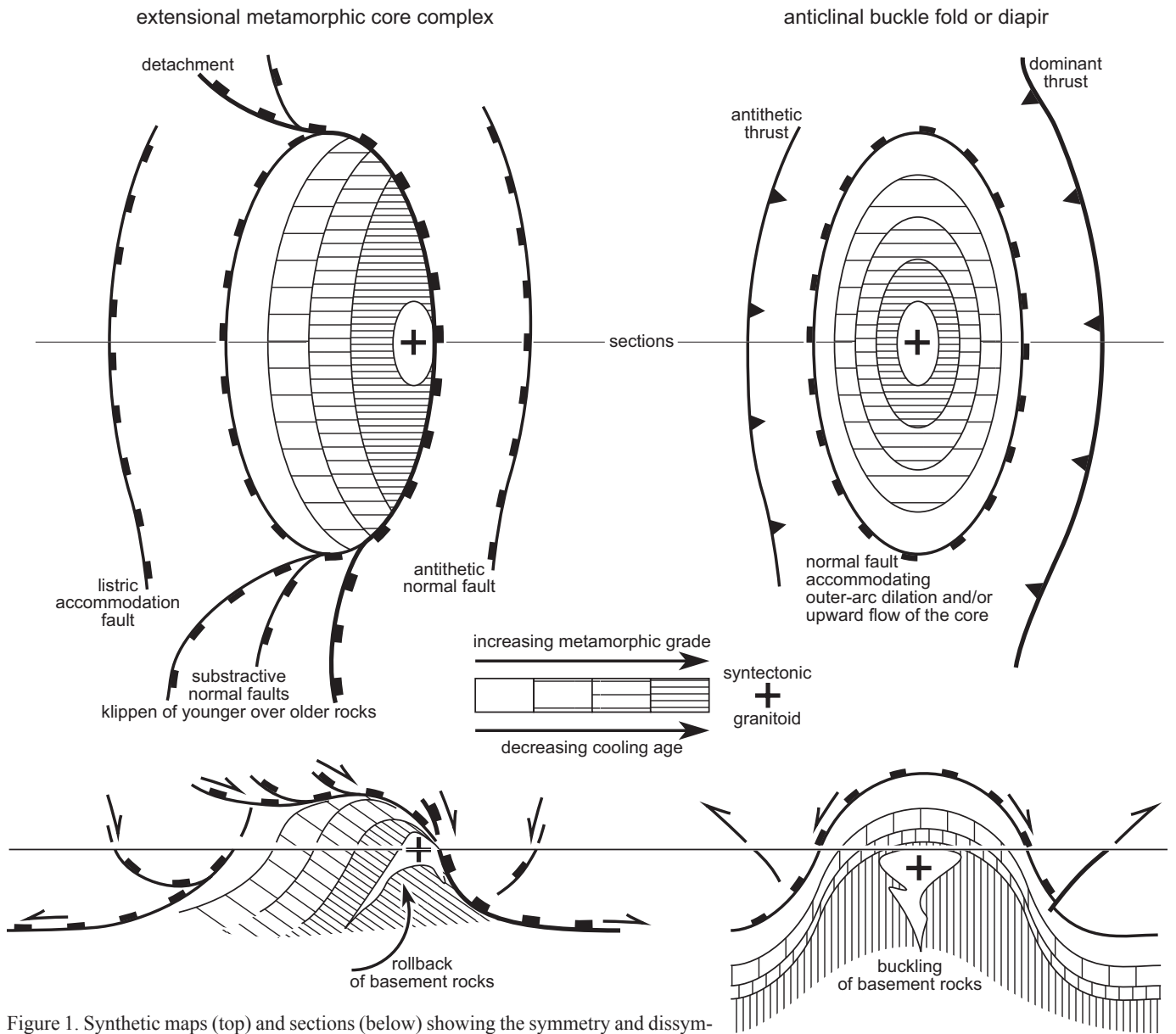


Figure 1. Synthetic maps (top) and sections (below) showing the symmetry and dissymmetry that characterize folds and diapirs on the one hand and extensional metamorphic core complexes on the other hand.

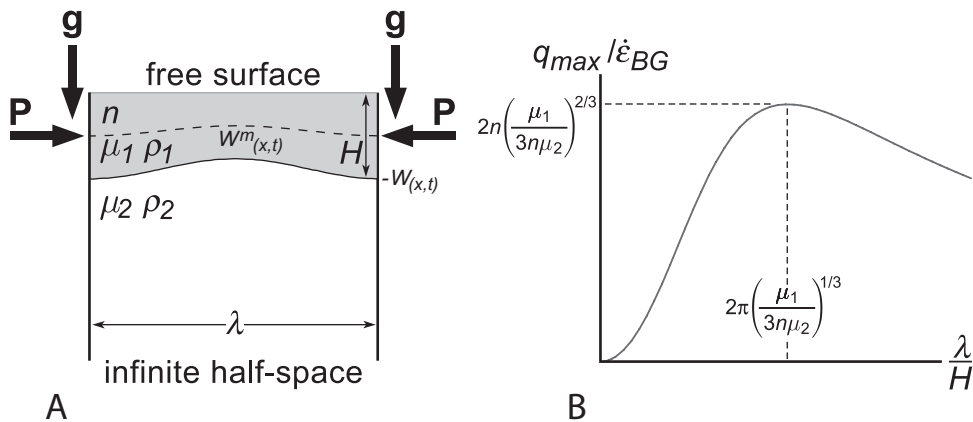


Figure 2. A. Setup for analytical investigation of a power law viscous plate floating on a linearly viscous half-space. B. Growth rate plotted versus normalized wavelength for the case without gravity. Definition for symbols provided in the text.

$$\frac{\mu_1}{3n} \frac{\partial^2}{\partial x^2} \left[H_\lambda(x)^3 \frac{\partial^3 W(x,t)}{\partial x^2 \partial t} \right] + \frac{\partial}{\partial x} \left[PH_\lambda(x) \frac{\partial W^m(x,t)}{\partial x} \right] - (\sigma_{Ntop} - \sigma_{Nbot}) = 0 \quad (1)$$

where μ_1 is the effective viscosity of the upper layer, n its power-law exponent, and P is the mean viscous layer-parallel stress, given by:

$$P = 4\mu_1 \dot{\epsilon}_{BG} \quad (2)$$

where $\dot{\epsilon}_{BG}$ is the background pure shear shortening rate (e.g., Turcotte and Schubert, 2002; Schmalholz et al., 2002).

$W(x,t)$ describes the deflection of the layer/halfspace interface, which is assumed to be sinusoidal with a time-dependent amplitude, $A(t)$:

$$W(x,t) = A(t) \sin(\omega x) \quad (3)$$

where $\omega = 2\pi/\lambda$ is the wavenumber. $W^m(x,t) = W(x,t)/2$ is the deflection of the middle line of the layer. $H_\lambda(x)$ is the thickness of the layer:

$$H_\lambda(x) = H - W(x,t) = H - A(t) \sin(\omega x), \quad (4)$$

where H is the mean thickness of the layer.

Finally, σ_{Ntop} and σ_{Nbot} are the vertical forces exerted at the top and bottom of the layer, respectively. The top is kept flat, so $\sigma_{Ntop} = 0$. The layer bottom is deflected and has a density contrast, so the vertical forces that act on the layer are due to the gravitational load and the viscous drag of the underlying halfspace with viscosity μ_2 (e.g., Turcotte and Schubert, 2002, Equation 6-165, p. 251):

$$\sigma_{Nbot} = 2\mu_2 \omega \frac{\partial W(x,t)}{\partial t} - (\rho_1 - \rho_2) g W(x,t) \quad (5)$$

in which ρ_2 and ρ_1 are the halfspace and layer densities, respectively.

Substituting equations (3), (4), and (5) into (1) and keeping only linear terms ($A(t)^2$ terms are omitted because $A(t)$ is assumed to be small) gives a linear ordinary differential equation (ODE) for the amplitude $A(t)$:

$$\frac{\mu_1 H^3 \omega^4}{3n} \frac{\partial A(t)}{\partial t} - \frac{P}{2} H \omega^2 A(t) + 2\mu_2 \omega \frac{\partial A(t)}{\partial t} - (\rho_1 - \rho_2) g A(t) = 0 \quad (6)$$

The solution of this ODE has the form $A(t) = A_0 e^{qt}$, where q is the growth rate, given by:

$$q = \frac{3n \left[\frac{PH\omega^2}{2} \right] + (\rho_1 - \rho_2)g}{\omega(\mu_1 H^3 \omega^3 + 6\mu_2 n)} \quad (7)$$

Substituting P from Equation (2) into Equation (7) yields:

$$\frac{q}{\dot{\epsilon}_{BG}} = \frac{3n \left[2\mu H \omega^2 + \frac{(\rho_1 - \rho_2)g}{\dot{\epsilon}_{BG}} \right]}{\omega(\mu_1 H^3 \omega^3 + 6\mu_2 n)} \quad (8)$$

Setting the gravity term g to zero yields a solution for folding without gravity. Plotting $q/\dot{\epsilon}_{BG}$ versus λ/H shows that this function has a single maximum growth rate (Fig. 2B) that can be found by setting the derivative of equation (8) versus ω to zero and solving for ω . The only positive solution for ω yields the so-called dominant wavelength (Biot, 1961; Ramberg and Stephansson, 1964)

$$\lambda_{dom} = 2\pi H \left[\frac{\mu_1}{3n\mu_2} \right]^{1/3} \quad (9)$$

with the corresponding growth rate:

$$q_{max} = 2n \left[\frac{\mu_1}{3n\mu_2} \right]^{2/3} \dot{\epsilon}_{BG} \quad (10)$$

Equation (9) shows that the dominant wavelength is dependent on the thickness of the layer and on the viscosity contrast between the upper and lower layers, a parameter that has a large amount of uncertainty in nature. Equation (10) shows that the growth rate is essentially dependent on the viscosity contrast. Note that the expressions for dominant wavelength and growth rate have a factor 3 in the denominator, which is appropriate for folding of one interface only.

It is interesting to compare these expressions with the solutions obtained for a folded upper surface without erosion (Schmalholz et al., 2002). The expressions for dominant wavelength are the same, but the dominant growth rate is smaller by a factor of two under fast erosion. This counterintuitive result, which was confirmed by more complete thick-plate analysis (Kaus, 2004), can be understood by noting that the folding instability is driven through deflections on interfaces between different layers. Since there is only one deflected interface in this setup, the rate at which the instability grows is half that when two interfaces are present. Another point worth noting is the effect of gravity. It can be seen from Equation (7) that a stable density configuration ($\rho_1 < \rho_2$) will decrease the growth rate, and a rather large density contrast will eliminate the folding instability. If the density configuration

is unstable ($\rho_1 > \rho_2$), calculations show that the dominant growth rate and wavelength both go to infinity (Kaus, 2004).

One should note that the above derivation has the implicit assumption that folds are periodic by inserting a sinusoidal interface deflection (Equation 3). However, the introduction of nonlinear effects in the matrix can result in a localized type of folding (e.g., Hunt et al., 1996). Both analogue (Abbassi and Mancktelow, 1992) and numerical (Zhang et al., 2000) experiments pointed out the strong localizing effect that finite amplitude initial perturbations have on the distribution and morphology of buckle folds.

The analysis presented above has been extended to large-scale problems by including the effects of a finite, low-viscous bottom layer called “matrix,” a denomination we will keep in this work to stay in line with earlier literature. Three different folding modes exist, depending on both the thickness of the lower viscous layer and the efficiency of gravitational versus compressional forces (Schmalholz et al., 2002). For example, gravity plays the dominant role in the lithospheric buckling of Central Asia, whereas the thickness of the underlying “soft” layer controls buckling in the Zagros and Jura mountains. In the following section, we further employ the setup described above (see also Goff et al., 1996).

MAGMATIC/DIAPIRIC DOMES

Geological Information

Diapirism and intrusion are the processes involved when a geological formation (the source layer) has come under sufficient stress (including gravity driven components) to flow, pierce, and break through overlying strata of higher density and strength. Magmas commonly have densities lower than those of the overlying rocks and consequently tend to ascend through passageways or zones of weakness. Most magma does not reach Earth’s surface but crystallizes at depth to form plutonic bodies of igneous rocks. If plutons are diapirs (a concept still disputed) magma stops rising where surrounding rocks have lower density

and/or at the temperature-equivalent depth where magma cools and solidifies (Vigneresse and Clemens, 2000; Burov et al., 2003). In fact, the coeval emplacement at similar depth of magmas with different composition indicates that there is no neutral buoyancy level in the crust. Accordingly, purely gravity-driven igneous diapirism does not exist (e.g., Vigneresse and Clemens, 2000). The abundance of pluton-cored domes in orogens, in particular in the European Variscides (Zwart, 1967), points to the participation of any tectonic deformation during magma ascent (Brun and Pons, 1981; Vigneresse and Clemens, 2000). A typical history comprises a deformation-controlled mechanical instability that becomes the location from which buoyant upwelling of relatively light magma starts, while “ballooning” characterizes final emplacement (Pitcher, 1979; Pons et al., 1992). A similar history is invoked for salt tectonics (e.g., Jackson and Talbot, 1989; Poliakov et al., 1996) and many migmatite domes (see discussion in Teyssier and Whitney, 2002). Diapiric ascent thus most often occurs in a regional tectonic setting whose actual role requires new investigations.

Mechanical Background

Here, we only summarize statements from previous work. The driving force of diapirism is the density inversion (Biot and Odé, 1965). The spontaneous rise of buoyant domes into a denser overburden in Earth’s gravity field is strongly inspired by salt tectonics (e.g., Talbot and Jackson, 1987). In its simplest form, the rock system consists of two horizontal layers, each of which has uniform thickness, density, and Newtonian viscosity (e.g., Woidt, 1978). Whether viscosities are equal or different, the setting is unstable if the overlying layer is denser than the lower one and the interface between the two layers is not perfectly flat. The gravitational instability of a heavy fluid overlying a lighter fluid is named Rayleigh-Taylor instability, which in its pure form is independent of background shortening or extension.

Dimensional analysis allows gaining a first insight in the basic parameters that control the Rayleigh-Taylor instability (Whitehead, 1988). A layer of thickness, H , density, ρ_2 , and

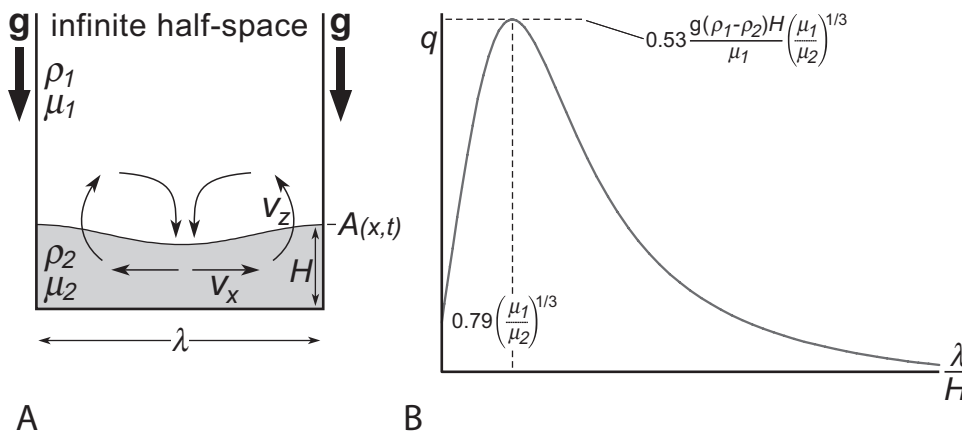


Figure 3. A. Setup for analytical investigation of a low-density viscous fluid underlying a higher density viscous halfspace. B. Growth rate plotted versus normalized wavelength. Definition for symbols provided in the text.

viscosity, μ_2 , underlies an infinite viscous halfspace (Fig. 3A). The horizontal velocity v_x in the layer is much larger than the vertical velocity v_z . Force balance in the layer is given by the lateral pressure gradient p :

$$\frac{p}{\lambda} = \mu_2 \frac{v_x}{H^2} \quad (11)$$

where λ is the wavelength of the sinusoidal perturbation on the interface separating the two fluids. The upper halfspace, with a viscosity μ_1 and density ρ_1 , will have a force balance between buoyancy, vertical velocity, and viscosity:

$$\frac{p}{\lambda} = \mu_1 \frac{v_z}{\lambda^2} + \frac{(\rho_1 - \rho_2)gA(t)}{\lambda} \quad (12)$$

where the density difference between the two layers is assumed to be >0 , g the gravitation acceleration and $A(t)$ the time-dependent amplitude of the perturbation. Combining Equations (11) and (12) gives:

$$\mu_2 \frac{v_x}{H^2} - \mu_1 \frac{v_z}{\lambda^2} = \frac{(\rho_1 - \rho_2)gA(t)}{\lambda} \quad (13)$$

Assuming further that the fluids are incompressible, (see Equation 6-53 in Turcotte and Schubert, 2002, p. 235):

$$\frac{\partial v_x}{\partial x} + \frac{\partial v_z}{\partial z} = 0$$

gives:

$$\frac{v_x}{\lambda} + \frac{v_z}{H} = 0 \quad (14)$$

Like for folding, the interface instability grows exponentially with time ($A(t) = A_0 e^{qt}$) at a growth rate q while the vertical velocity increases the amplitude as expressed by:

$$v_z = \frac{\partial A(t)}{\partial t} \quad (15)$$

where $\partial/\partial t$ expresses the time derivative. Substituting Equations (14) and (15) in (13) gives:

$$\left[\frac{\mu_2 \lambda}{H^3} + \frac{\mu_1}{\lambda^2} \right] q A_0 e^{qt} = - \frac{(\rho_1 - \rho_2)gA_0 e^{qt}}{\lambda} \quad (16)$$

and solving for q :

$$q = - \frac{(\rho_1 - \rho_2)g}{\lambda \left[\frac{\mu_2 \lambda}{H^3} + \frac{\mu_1}{\lambda^2} \right]} \quad (17)$$

This simple derivation shows that the growth rate depends on the wavelength of the perturbation (Whitehead, 1988). Figure 3B plots the growth rate as a function of normalized wavelength (λ/H). For the specific wavelength/thickness ratio:

$$\frac{\lambda_{dom}}{H} = 0.79 \left[\frac{\mu_1}{\mu_2} \right]^{1/3} \quad (18)$$

the growth rate is maximum:

$$q = 0.53 \frac{g(\rho_1 - \rho_2)H}{\mu_1} \left[\frac{\mu_1}{\mu_2} \right]^{1/3} \quad (19)$$

This equation predicts the most favorable condition for the development of Rayleigh-Taylor instabilities (pure diapir). More complete derivations using a two-dimensional perturbation analysis also reach this basic result (Whitehead, 1988), albeit with different coefficients. The notable conclusions gained from this analysis are:

- The viscosity contrast is the chief parameter controlling the wavelength of a diapiric instability. As such, the dependence of the dominant wavelength on viscosity is the same as for folding of a viscous layer in a viscous matrix (see Equations 9 and 10).
- Density influences the growth rate only and has a negligible effect on the wavelength.

ANALYTICAL PERTURBATION METHOD

Several authors have considered the case of a Rayleigh-Taylor instability under compression and demonstrated that above a certain strain rate the folding instability becomes dominant (e.g., Conrad and Molnar, 1997; Ismail-Zadeh et al., 2002). To solve our geological preoccupation, which is how to tell fold-domes from diapir-domes, we decided to explore the transition between both instability modes. We addressed the problem by using three methods for the simplest, two-layer system. First, the analytical perturbation method, which is valid for the onset of both types of instability, is used to derive a “phase diagram,” discriminating different modes of deformation. Second, numerical simulations were performed to test the applicability of the phase diagram and to study the geometries that develop during the nonlinear finite amplitude stages. Finally, we calculated and compared the patterns of finite strain, which geologists may be able to use to distinguish the different deformation modes from field observations.

Method

In order to get insight into the transition between diapirism and buckling modes, the simplest model consists of a layer of high viscosity and density over a layer with lower viscosity and density (Fig. 4). The system is subjected to layer-parallel, pure-shear background deformation at a constant strain rate. Gravity is present. The bottom boundary is rigid (no-slip condition), and the top is a fast redistribution boundary (no stress condition on the top boundary kept flat throughout experiments). Rheology is assumed to be linearly viscous. With this setup, a standard perturbation method (e.g., Fletcher, 1977; Smith, 1977) was employed to derive an analytical solution that describes the growth rate of the layer interface as a function of its wavelength, density and viscosity structure, and the thickness of both layers (see Appendix). The complete analytical solution is rather complicated and grants only limited insight on the controlling parameters. Therefore, analytical solutions regarding the dominant wavelength and growth rate were obtained for several end-member cases. For instance, an expression for dominant growth rate and wavelength was derived in the case of thin-layer diapirism by setting the background strain rate to zero and making the lower layer much thinner than the upper layer. The result obtained in this way is similar to that derived for magmatic/diapiric domes on the basis of dimensional analysis (Equations 18 and 19).

Phase Diagram: Folding versus Diapirism

With the technique summarized above, eight deformation modes could be distinguished, each with a different expression of dominant growth rate and wavelength. These deformation modes are displayed in a two-dimensional phase diagram (Fig. 5) using two non-dimensional numbers, B and B_{det} , constructed

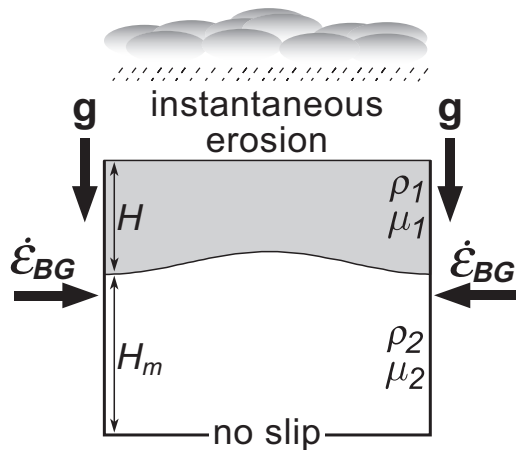


Figure 4. Setup used in this work. A layer of high viscosity and density lies over a layer with lower viscosity and density. The system is subjected to layer-parallel, pure-shear background deformation at a constant strain rate. Gravity is present. The bottom boundary is rigid and the top is kept flat. Definition for symbols provided in the text.

on the basis of rheological and geometrical parameters (Kaus 2004). They are:

$$B_{det} = \left[\frac{H_m}{H} \right] R^{-1/3} \quad (20)$$

$$B = 0.39(Ar)R^{-2/3}$$

where R is the viscosity contrast (μ_1/μ_2) between the upper and the lower (matrix) layer, respectively, H and H_m the thickness of the lower and upper layer, respectively, and Ar the Argand number expressing the importance of gravity over background shortening rate $\dot{\epsilon}_{BG}$ (adapted from England and McKenzie, 1982):

$$Ar = \frac{(\rho_1 - \rho_2)gH_m}{2\mu_2\dot{\epsilon}_{BG}} \quad (21)$$

Note that this definition of the Argand number differs from both the original definition (England and McKenzie, 1982) and that employed by Schmalholz et al. (2002). This point emphasizes that the definition of the Argand number is problem-related. With Equation (21), gravity dominates over compression if the Argand number (and therefore the B number) is large, and one expects diapiric-type structures. On the other hand, low Argand numbers indicate folding or homogeneous thickening modes.

Contours of the dominant growth rate and dominant wavelength versus B and B_{det} are shown in Figure 5. The curves of iso-dominant wavelength and/or iso-growth rate have different slopes in different regions of the diagram, thus defining eight fields. The mechanical “phase-boundaries” are the locus of the points where slopes change. Inside each field, the growth rate of the given mode is larger than the growth rate of any of the other seven modes.

It can be readily seen that diapiric modes (gravity dominated) roughly occur for $B > 1$, and folding modes (where compression dominates) exist when $B < 1$. Somewhat expectedly, the transition depends largely on the Argand number.

Three fields cover the diapiric modes:

1. Thin-layer diapirism, when the interlayer boundary is very close to the bottom, no-slip boundary;
2. Detachment diapirism, when the interlayer boundary is further up from the bottom, which still influences the dynamics of the system;
3. Matrix diapirism, when the stiff and thin top-layer exerts no influence.

Five fields cover the folding modes. With increasing B_{det} numbers, they are:

1. Thin layer folding, when the interlayer boundary is very close to the bottom boundary. In this case, growth rates are slower than the background shortening-rate. Folds will still grow, but at such a slow rate that they will not become discernable during the later stages.
2. Detachment folding, when the interface is further up from the bottom, but the influence of the bottom is still felt. The

low-viscosity lower layer acts like a thin channel and the growth rate of the interlayer boundary is limited by the rate with which viscous fluids can flow through this channel. Therefore, growth rates increase with increasing channel thickness (i.e., increasing B_{det} number).

3. Matrix folding, when the lower layer is thick enough to act like an infinite matrix (halfspace). Growth rates depend solely on the viscosity contrast and background strain rates.

4. Detachment erosion, which has significantly longer dominant wavelengths than the matrix-folding field. The growth rates are sensitive to viscosity contrast, matrix thickness, and background strain rate.

5. Matrix erosion, which is not dependent on the thickness of the top stiff and thin layer.

In light of previous work (Schmalholz et al., 2002), the folding modes 1, 2, and 3 were expected. The new modes, 4 and 5, are due to the action of erosion. The growth rate curves of these two compression modes draw attention because they have two maxima. For small B_{det} numbers (modes 1–3), the first maximum always dominates. However, if B_{det} becomes larger than $10^{1.2}$ (for $R = 100$), the second peak overtakes the first (insets in Fig. 5B). This is accompanied by a sudden increase in dominant wavelength.

Not all of the eight fields on the phase diagram are expected to occur in nature. The thin-layer folding field is one example. The growth rate is always smaller than background shortening, implying that the system will deform homogeneously rather than produce a localized instability. The erosion modes that require

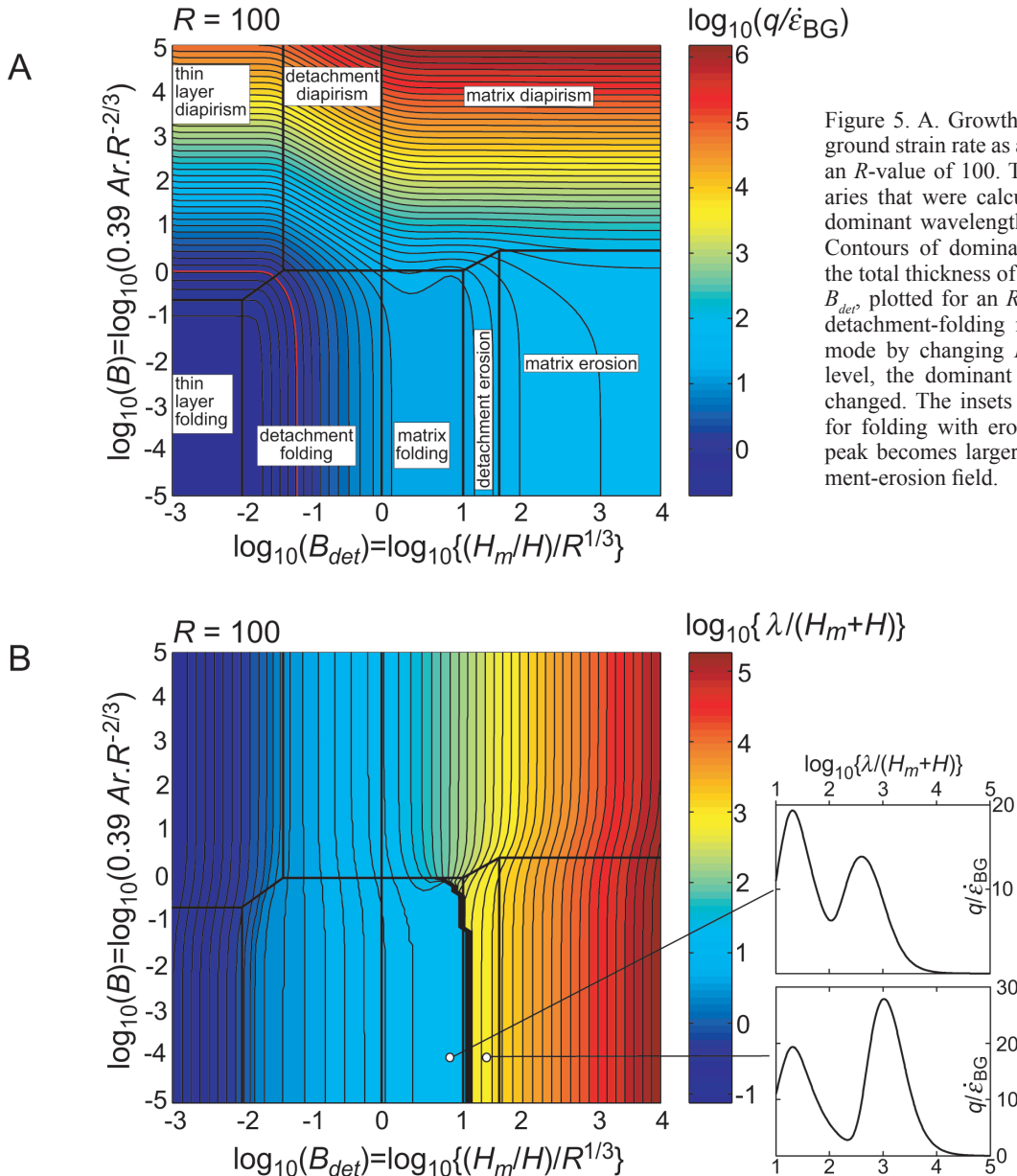


Figure 5. A. Growth rates normalized over the background strain rate as a function of B and B_{det} plotted for an R -value of 100. Thick lines indicate phase boundaries that were calculated on the basis of simplified dominant wavelength and growth rate expression. B. Contours of dominant wavelengths normalized over the total thickness of the system as a function of B and B_{det} plotted for an R -value of 100. Switching from a detachment-folding mode to a detachment-diapirism mode by changing B but keeping B_{det} at a constant level, the dominant wavelength remains almost unchanged. The insets show that the growth rate curve for folding with erosion has two peaks. The second peak becomes larger than the first one in the detachment-erosion field.

very large thickness ratios are another example. Consider, for example, a 50 km thick crust. If a viscosity contrast of 100 is assumed between a strong upper crust and a weak lower crust, the thickness of the strong layer should be around 350 m in order to fall within the detachment-erosion mode ($\log_{10} B_{det} = 1.5$). Esti-

mates of the effective thickness of the upper crust for Central Asia vary between 6 and 12 km (Schmalholz et al., 2002). Owing to these limits, only 5 fields are considered further in the current study (Fig. 6A). Changing the viscosity contrast affects the topology of the phase diagram (Fig. 6B). The boundaries between the diapiric modes 2 and 3 and between the folding modes 2 and 3 are independent of the viscosity contrast, a fact due to the definition of B and B_{det} . The other boundaries move across the diagram so that the other fields widen with increasing viscosity contrast.

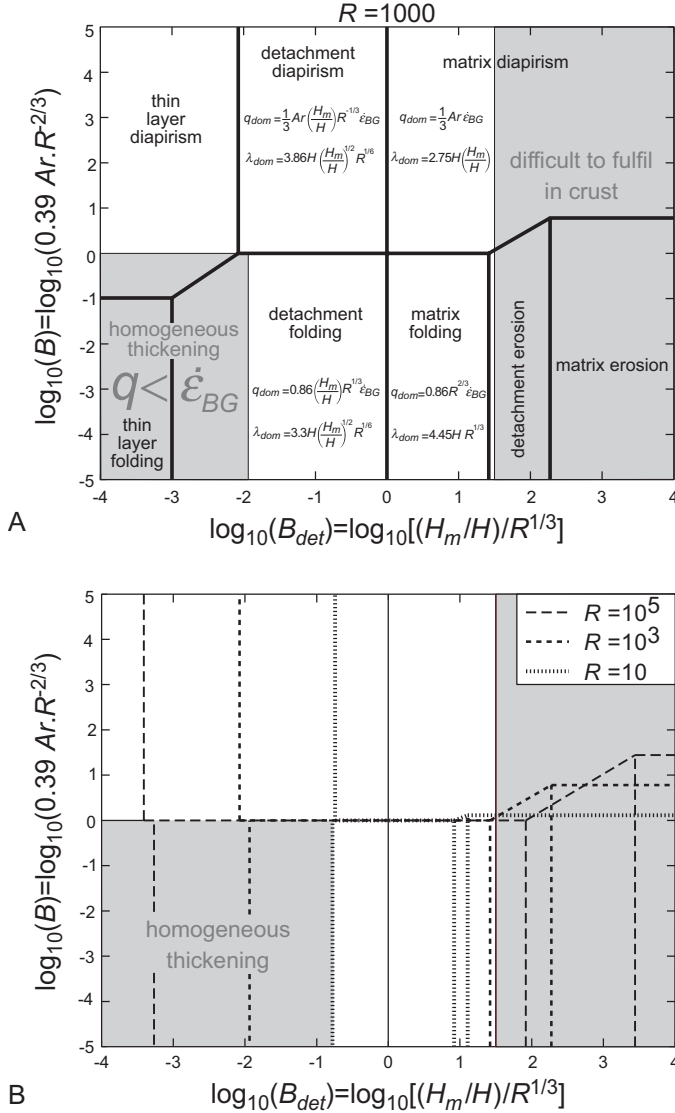


Figure 6. A. Phase diagram for crustal deformation for a viscosity contrast of $R = 1000$ as a function of B and B_{det} . Not all phase fields are likely to occur at crustal scale, because some require a very thin layer on a very thick matrix (detachment erosion and matrix erosion fields) and others have a growth rate smaller than the background shortening-rate (thin-layer folding) and will therefore not produce finite amplitude domes. B. Topology of the phase diagram as a function of viscosity contrasts. The non-dimensional numbers B and B_{det} were chosen in such a way that the boundary between the four fields that are thought to be relevant for the crust is independent on the viscosity contrast. The other fields become larger with increasing viscosity contrast.

Discussion

The first point extractable from the phase diagram (Fig. 5) is that detachment folding and detachment diapirism have very similar dominant wavelengths. For example, consider a model with given layer thicknesses and viscosity contrast resulting in $\log_{10} B_{det} = -1$. If compression is very slow (i.e., $\dot{\epsilon} \rightarrow 0$), the Argand number is very large ($Ar \rightarrow \infty$) and, consequently, the B number is large. A diapiric, purely gravity-driven deformation mode will develop with a given wavelength (Fig. 5B). If the system now suddenly undergoes compression, the B number decreases and detachment folding becomes favored. However, the dominant wavelength remains almost unchanged and instabilities that started forming in the diapiric field are likely to continue amplifying under the folding mode without discernable consequences on the wavelength. This observation may help in understanding sites and shapes of salt diapirs that pierce periodical folds of the Zagros Mountains (Alavi, 1994). A second point is that the shapes of both diapirs and folds developing while being instantaneously eroded have two-dimensional profiles that look alike; both have chimney (cusp) shapes with very steep walls and narrow heads. The three dimensional shape of the resulting structures is only partially understood for diapirs. Three dimensional, tubular diapirs amplify slightly faster than two-dimensional, linear, wall-like diapirs at finite amplitudes (Kaus and Podladchikov, 2001). Therefore, diapirs tend to form finger-like (or in map-view, circular) intrusions. Three-dimensional folding, on the other hand, has only been studied in the linear initial stages for a layer embedded in an infinite matrix (Fletcher, 1991, 1995). The effects of both finite amplitude and a detachment layer remain to be examined. At the moment, we can only speculate that existing large-amplitude three-dimensional folds will continue amplifying in the same detachment-folding mode.

NUMERICAL SIMULATION

The boundaries separating the different deformation modes are relatively sharp (Fig. 5), which points to rapid changes in deformation mechanism from one mode to the next. However, the analytical perturbation method used to derive the diagram has an important shortcoming in that it implies infinitely small perturbations of the interface and, therefore, is valid only for starting conditions. Linearization is too strong an assumption for understanding geological structures that accumulate large

amounts of strain. We performed numerical simulations to study the importance of nonlinear finite amplitude effects and, therefore, to estimate the validity of the analytical predictions.

Numerical Technique

We used the code GANGO (Kaus, 2004), which is a two-dimensional Eulerian finite-difference/spectral method that builds upon the technique described in Schmalholz et al. (2001). It solves the momentum equations for the slow motion of rocks on geological timescales. Incompressibility is assumed. The gov-

erning partial differential equations are solved on a two-dimensional domain that uses a spectral approximation in the horizontal direction and a conservative finite difference approximation in the vertical direction. Time stepping is done with an implicit algorithm in order to accurately track the highly unstable initial stages of the developing instabilities. A marker line that eliminates numerical diffusion describes the interface between layers of different, sharply varying material parameters.

The two-layer setup is the same as that used for the analytical method (Fig. 4). It mimics a high-viscosity, high-density layer, analogue to the upper crust, resting on a low-viscosity,

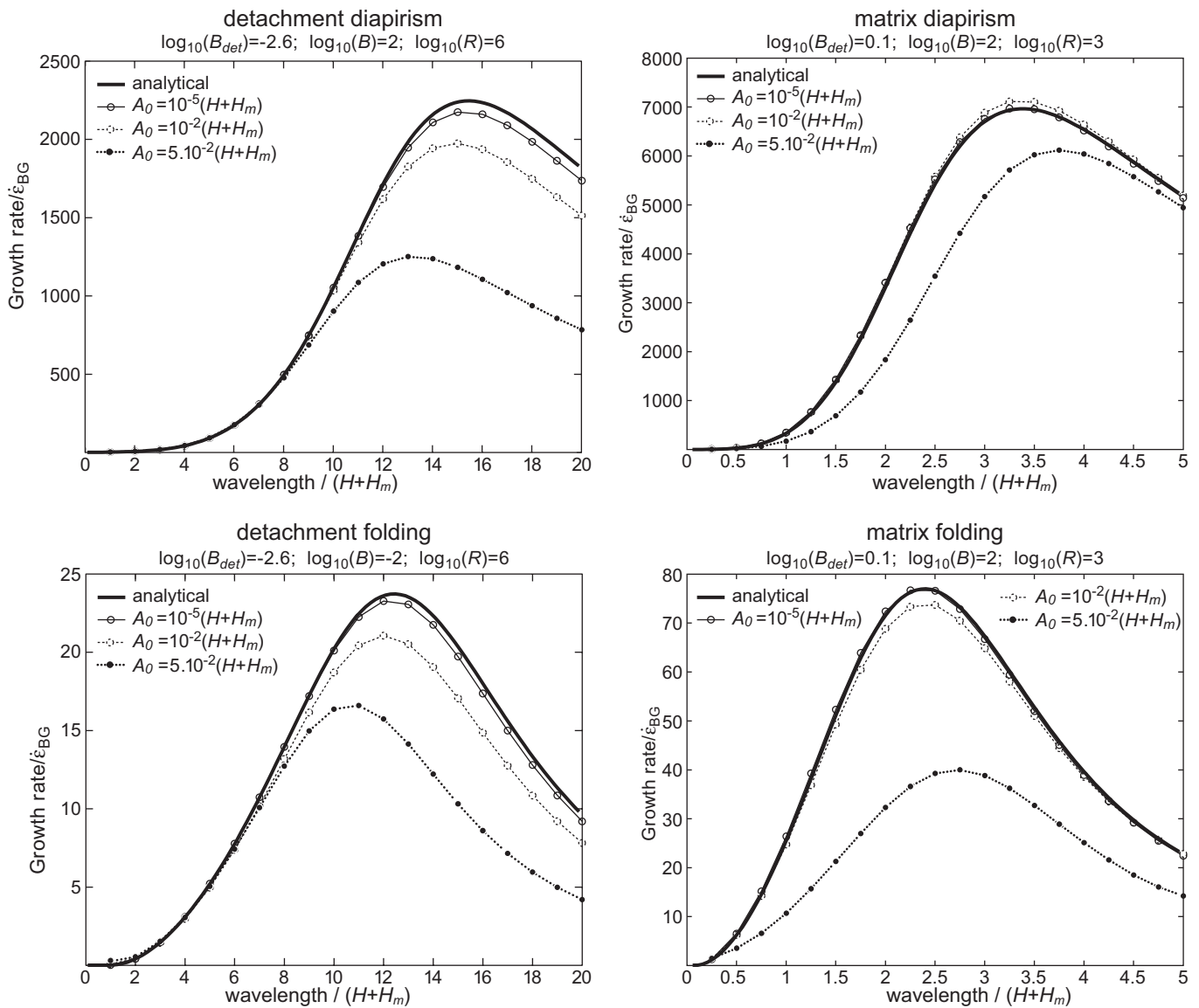


Figure 7. Comparison of analytical growth rates with numerically determined growth rates for four different deformation modes. In all cases, the numerically determined growth rates with a small amplitude perturbation are very close to analytical results. Cases where the initial perturbation has larger amplitude generally result in smaller growth rates, while the dominant wavelength remains almost unchanged.

low-density layer representing the deeper crust. The density inversion could represent, for example, magma-rich migmatites or salt at depth. Rheology is linearly viscous and constant within each layer. Horizontal boundary conditions are assumed to be periodic on top of a background pure-shear velocity field. A no-slip boundary condition was set at the bottom boundary; fast redistribution is allowed on the top boundary. This means that the topography created at the surface is instantaneously flattened; depressions are filled with a high-viscosity, high-density material similar to that of the upper layer. Thus, the modeling particularly concerns regions of very fast erosion and sedimentation, as is suggested in the Himalayan syntaxes (Burg and Podladchikov, 2000).

Comparison of Numerics and Analytics

In order to check the accuracy of the code, we numerically calculated growth rates by imposing different sinusoidal perturbations of small amplitude at the interlayer boundary and recording the fastest growth rate under four different deformation modes, detachment and matrix diapirism, and detachment and matrix folding. The analytical and numerical results show a good agreement (Fig. 7). To study the nonlinear finite amplitude effects, growth rates were calculated for sinusoidal perturbations with larger initial amplitudes. In this case, the growth rate curves are similar in shape, but the magnitudes are smaller. Therefore, the dominant wavelength of finite amplitude instabilities is close to the wavelength predicted by the analytical solution. Accordingly, the phase diagram can be applied to large strain cases.

Geometries Developing at Finite Amplitude Stages

Previous numerical simulations have demonstrated that an initially horizontal layer perturbed with random noise develops structures with wavelengths close to the dominant wavelength (e.g., Schmalholz and Podladchikov, 1999; Kaus and Podladchikov, 2001). Exceptions to this general rule can occur if the amplitude of the noise is large compared to the thickness of the layer (e.g., Mancktelow, 1999), if a large non-dominant initial perturbation is present (e.g., Schmeling, 1987), or if the dominant growth rate is smaller than the background strain rate. Simulations starting with an initial low-amplitude random noise performed for four deformation modes (not shown here, see in Kaus, 2004) indeed developed into structures with a wavelength close to the dominant one. To study the geometries developing during finite amplitude stages, it is therefore sufficient to start with a sinusoidal perturbation of dominant wavelength. Results of such calculations are displayed in Figure 8, for which, in addition to the B and B_{det} numbers, the initial perturbation amplitude was varied. Figure 9 shows simulations for the same B and B_{det} parameters with different viscosity contrasts. The resulting structural characteristics can be summarized as follows:

- *Thin-layer diapirism to detachment diapirism*: a tendency to form balloon-on-a-string diapirs (Podladchikov

et al., 1993) is observed, both at small and large initial amplitudes and viscosity contrasts. After the diapir reaches the surface, its form changes to a stock or chimney-like shape.

- *Detachment diapirism*: Simulations with a viscosity contrast of 3000 always produced chimney-like geometries after the low-viscosity low-density material reaches the surface. The simulation with a lower viscosity contrast formed a balloon-on-a-string diapir. The smaller dominant wavelength and thickness ratio in this simulation than in the other cases explains this difference. The interface is far from the eroding top surface during the initial stages, and the shape of the diapir evolves as if the top were a no-slip or free-slip boundary (e.g., Woidt, 1978). Additional simulations showed that, as a rule-of-a-thumb, chimney-like diapirs form if the dominant wavelength is at least 4–5 times larger than the thickness of overburden.
- *Matrix diapirism*: All simulations evolve toward chimney-like structures.
- *Thin-layer folding to detachment folding*: Dynamic growth rates are too small to have active amplification of the interlayer surface whose change in shape is due to the overall pure-shear shortening.
- *Detachment folding*: The simulation with a small initial amplitude and large viscosity contrast has active amplification but insufficient to reach the surface. The thereby developed “hidden” chimney-like structure would be difficult to observe in orogenic belts. Simulations that started with a larger initial amplitude, on the other hand, produced structures that reached the surface, after which the geometry evolved toward chimney-like structures. Simulations with a smaller viscosity contrast have smaller growth rates and no active amplification.
- *Matrix folding*: All simulations reach the surface and form chimney structures very similar to those in the matrix-diapirism field.

In conclusion, two different dome-like geometries can be observed: (1) the classical diapir structure, which forms if very thin layers are present; and (2) chimney-like structures, which form both in folding and diapiric deformation modes.

Dynamics of Dome Formation

Numerical results show that the final stage morphology of both diapiric and folding deformation modes are very similar, at least regarding the shape of the interface between different material properties. The aim of this section is to investigate differences in the dynamic evolution of buckling and diapiric deformations. Figure 10 shows snapshots in the evolution of a simulation in the detachment diapirism field and in the detachment-folding field. Comparisons are made for the stream function and effective stress (second invariant of the deviatoric stress tensor; e.g., Ranalli, 1995). During the first two stages, before the growing structures reach the surface, the velocity patterns are very similar. Both diapirs and folds behave as

if the low-viscosity material flows through a thin channel toward the center of the dome. However, differences exist in the magnitude and distribution of effective stress; much larger values are built up in the folding mode, which is due to larger background strain rates set in this simulation.

During the last stages, after the interlayer boundary reaches the surface, considerable differences occur in the velocity field. Upward flow in the center of the eroding dome continues in the diapiric mode, with acceleration due to the fact that velocities are no longer controlled by the highest but by the lowest viscosity region. Folds, however, change the velocity pattern from

upward movement to downward squeezing of low viscosity material near the center of the dome. This is accompanied with a decrease in absolute velocity and can be explained because the dominant mechanism changes from a folding instability to flow-between-rigid-plates. If this channel has a wedge-shaped form, the material gets squeezed outward rather than through the channel. Simulations within the matrix-dominated fields confirm these results: Initial velocity patterns are similar, but patterns change once erosion of the dome material starts.

Chimney-like structures are appealing features to explain the formation of isolated domes because the so-called dominant

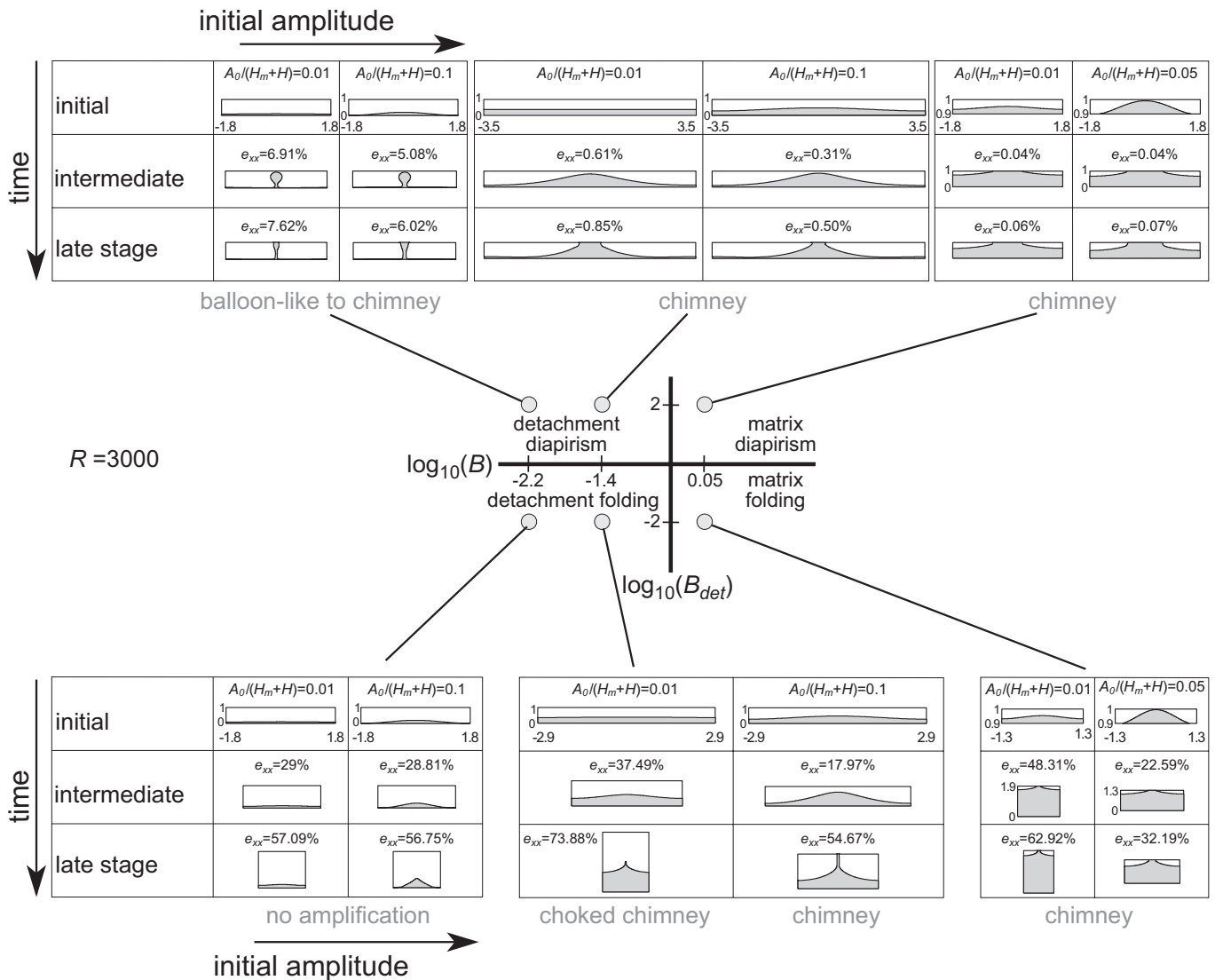


Figure 8. Geometrical results of numerical simulations for the four deformation modes relevant for crustal-scale deformation. The viscosity contrast R is 3000 in all simulations. The initial setup has a sinusoidal perturbation whose wavelength is the dominant wavelength. Two simulations were performed at specific (B, B_{det}) points: one with initial amplitude, A_0 , of 0.01 times the height of the initial box and one with larger initial amplitude. Varying the initial amplitude has relatively little effect on the final structures that form in the detachment-diapirism, the matrix diapirism, and the matrix folding fields, whereas it has significant effect in the detachment-folding field where the anticlinal crest does not always reach the surface. e_{xx} —shortening in the horizontal (x) direction.

wavelength becomes very large under rapid erosion conditions. These two aspects, along with the occurrence of steep limbs, are reminiscent of the Himalayan Syntaxes. However, the bulk form and distribution are scantily discriminating. Therefore, we tried to establish further discrimination between diapirs and folds from the strain field in and around domes.

STRAIN IN AND AROUND DOMES

In order to predict the strain distribution in and around domes, a feature observable to geologists, a passive grid was inserted in

the numerical simulations and moved with the calculated velocity distributions. Results are displayed in the form of finite strain ellipsoids for an intermediate stage in Figure 11 and for a late stage in Figure 12, which are chosen for their likeliness in the shape of the interface. Expectedly, the largest strains are recorded within the low viscosity materials. Diapir simulations show a normal sense of shear toward the diapir-overburden interface. The matrix-folding simulations show a reverse sense of shear toward this interface, which is in agreement with fold vergence and the senses of shear that geologists have been using (Figs. 13 and 14). However the detachment folding simulations behave

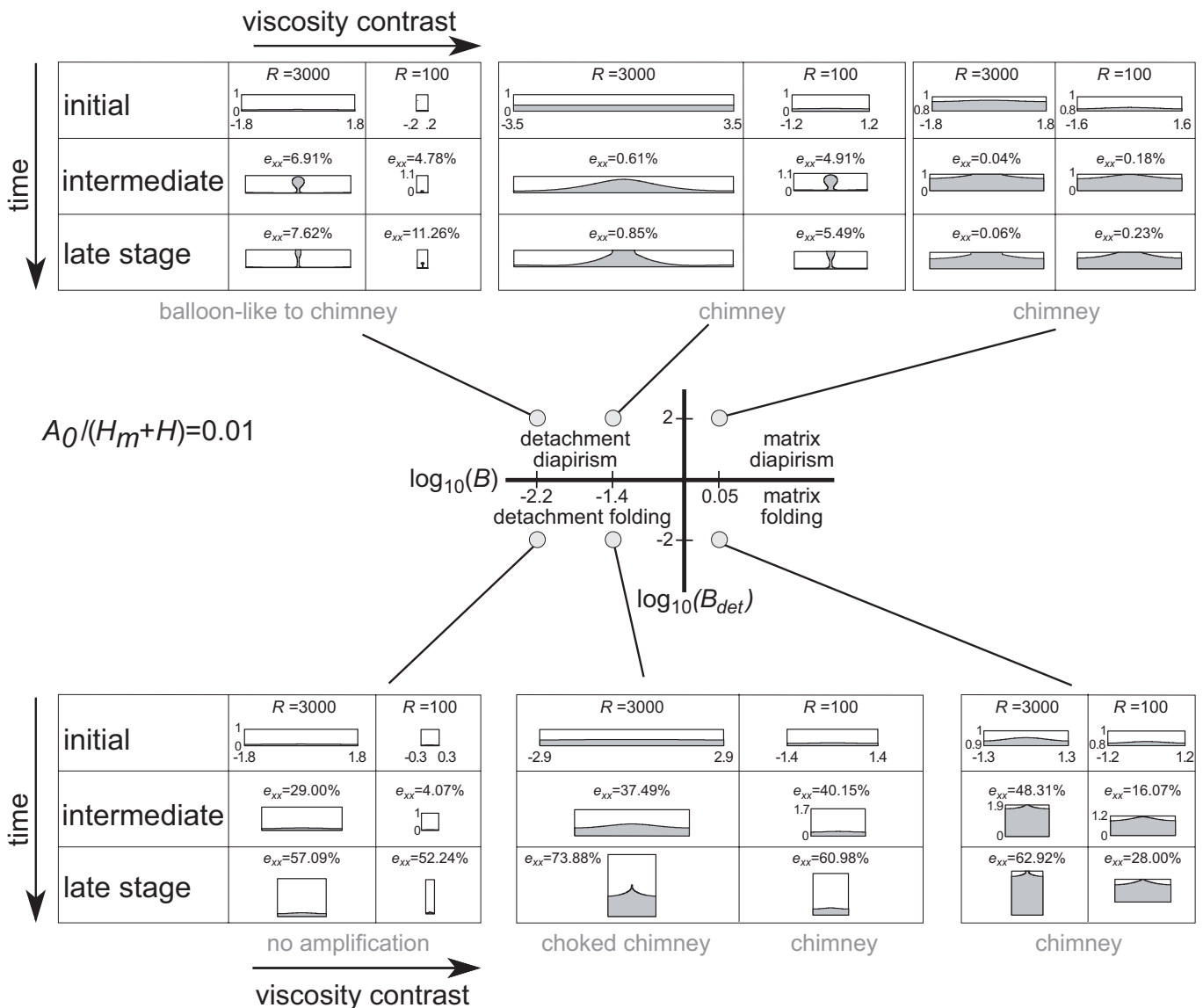


Figure 9. Results of numerical simulations where the viscosity ratio between the dense, high viscosity layer (white) and a lighter, low viscosity layer (gray) is varied. The initial amplitude is set to 0.01 times the box thickness. All other parameters are the same as in Figure 8. e_{xx} —shortening in the horizontal (x) direction.

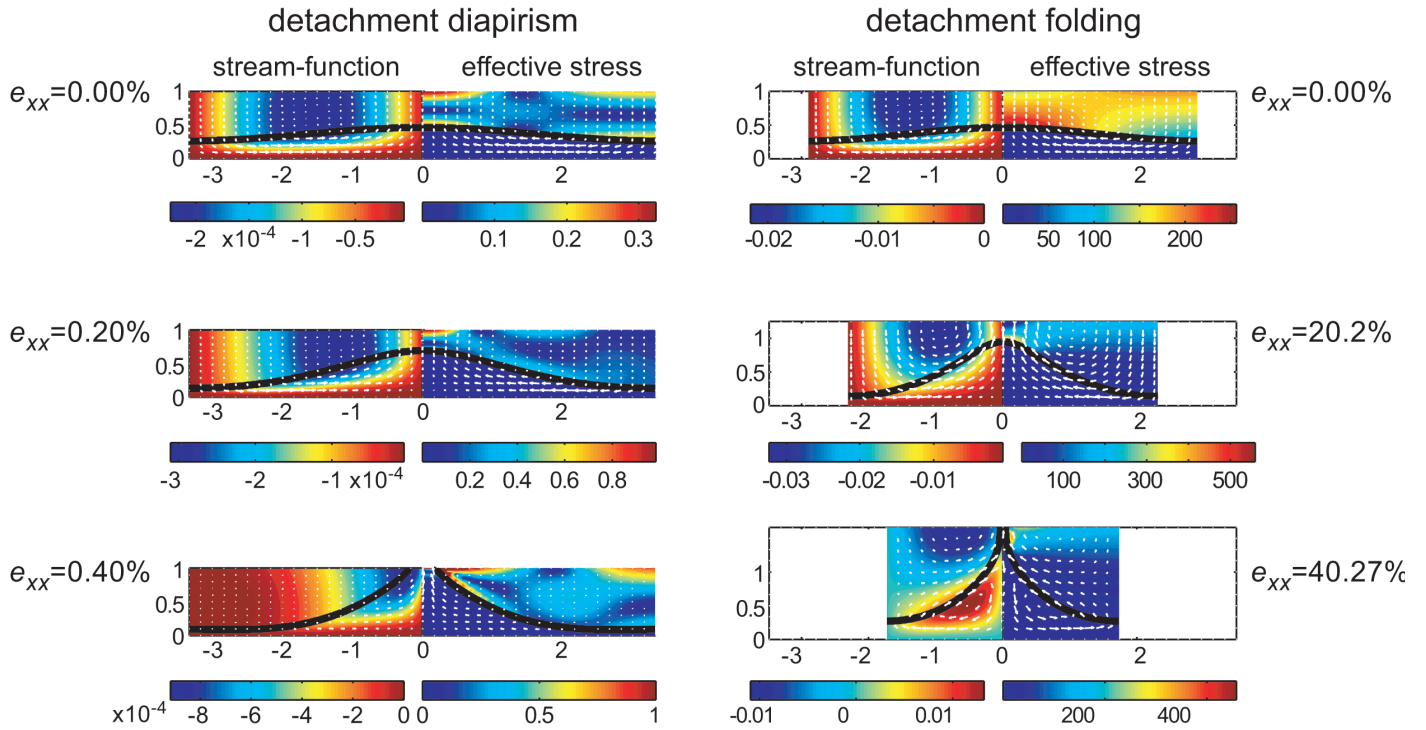


Figure 10. Results of numerical calculations, showing different snapshots of a simulation in the detachment diapirism field ($B_{det}=10^{-1.4}$, $B=10^2$) and a simulation in the detachment folding field ($B_{det}=10^{-1.4}$, $B=10^2$). Colors indicate stream function (left) and effective stress (right). White arrows indicate active velocity (i.e., velocity minus background pure-shear velocity). The viscosity contrast R is set to 3000 and the initial amplitude A_0 is 0.1 times the height of the box. During the initial stages, the main difference between folding and diapirism is the magnitude of effective stress in the high viscous layer, which is due to the fact that the background strain rate is larger in the folding case. Remarkably, the active velocity field and the geometry of the interface are similar for both cases. Only after the low viscosity/low density material has reached the surface and is being eroded, the deformation pattern changes significantly: Whereas the diapir continues to move upward with a dramatically increased rate, the material in the core of the fold mainly follows a downward movement (gets squeezed away). e_{xx} —shortening in the horizontal (x) direction.

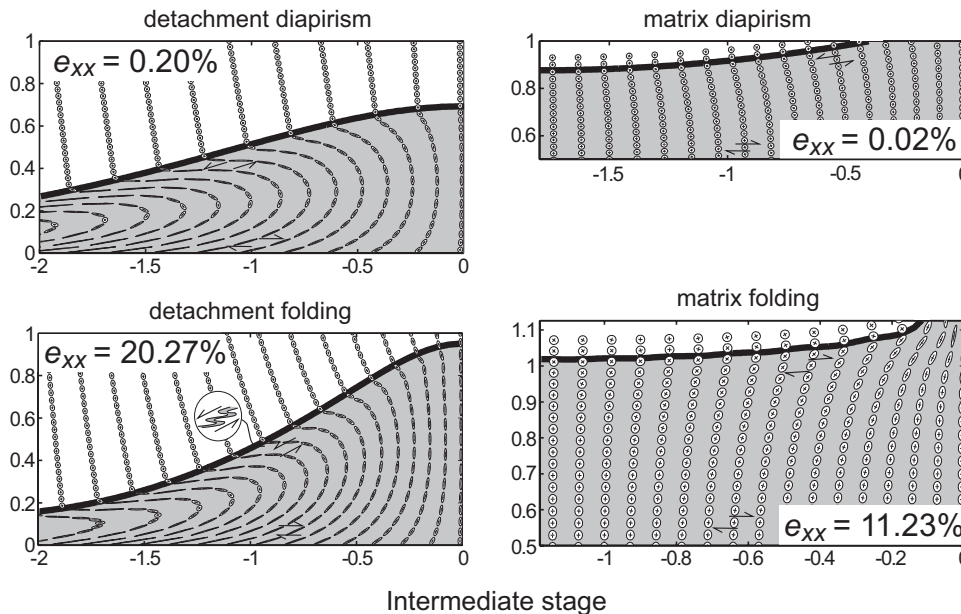


Figure 11. Strain patterns around diapirs (top) and folds (bottom) during intermediate stages when the low viscosity material has not yet reached the surface. The following parameters were used: detachment diapirism, $\log_{10}(B_{det})=-1.4$, $\log_{10}(B)=2$, $R=3000$, $A_0/(H+H_m)=0.1$; matrix diapirism, $\log_{10}(B_{det})=0.05$, $\log_{10}(B)=2$, $R=3000$, $A_0/(H+H_m)=0.1$; detachment folding, $\log_{10}(B_{det})=-1.4$, $\log_{10}(B)=2$, $R=3000$, $A_0/(H+H_m)=0.1$; and matrix folding, $\log_{10}(B_{det})=0.05$, $\log_{10}(B)=2$, $R=3000$, $A_0/(H+H_m)=0.1$. Both detachment folding and detachment diapirism show a very similar strain pattern, which resembles the pattern classically attributed to diapirs only. e_{xx} —shortening in the horizontal (x) direction.

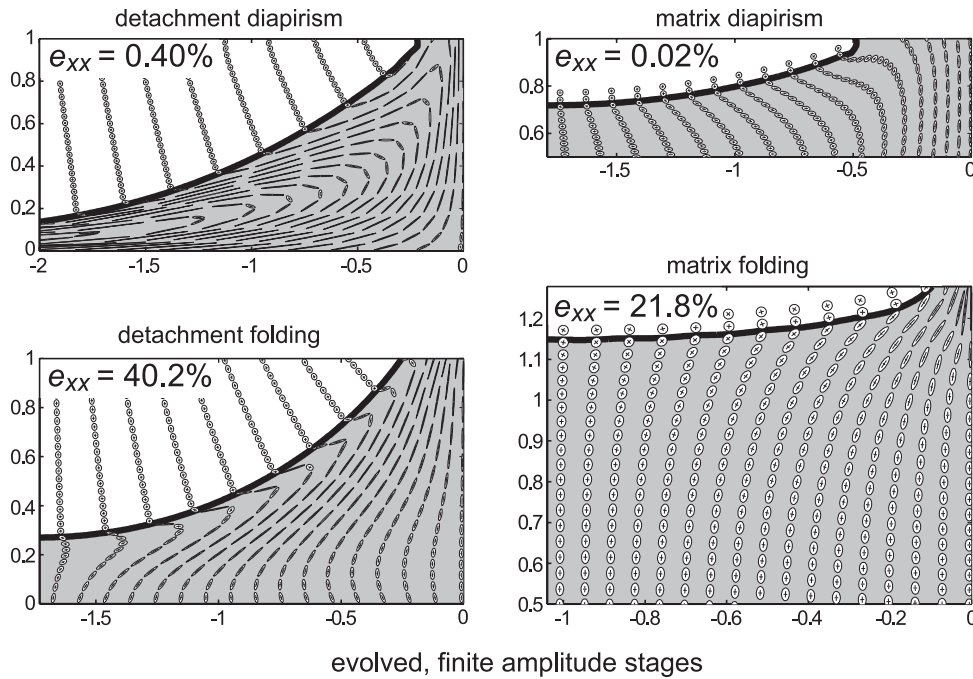


Figure 12. Strain patterns around diapirs (top) and folds (bottom) during late stages, when the low viscosity material has reached the surface and is being eroded. All parameters are the same as in Figure 11. Matrix folding and matrix diapirism still have opposite senses of shear close to the boundary. Detachment diapirism and detachment folding have the same sense of shear close to the interface; however, the detachment folding sense-of shear flips toward the center of the anticline. e_{xx} —shortening in the horizontal (x) direction.

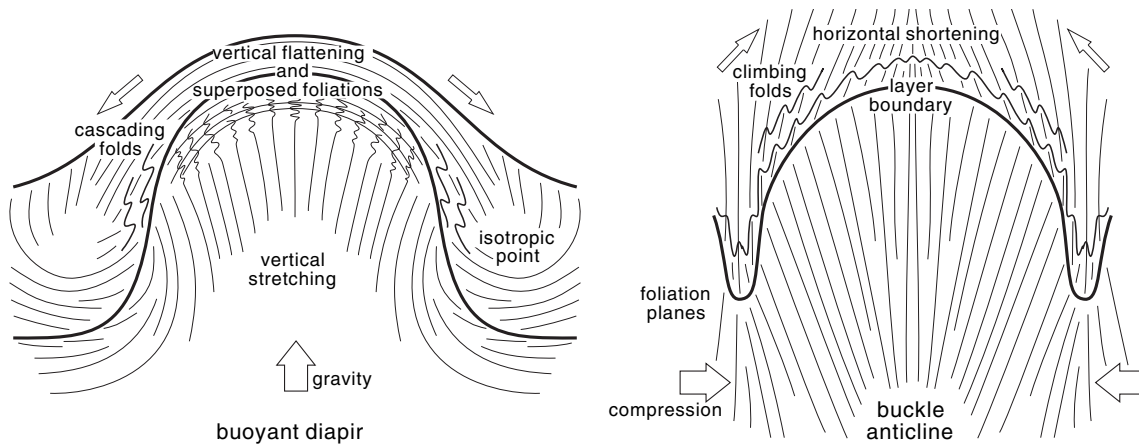


Figure 13. Structural characteristics of a cylindrical diapir and a cylindrical buckle-anticline; adapted from Dixon (1987). This classical morphology is consistent with matrix diapirism and folding (Fig. 12).

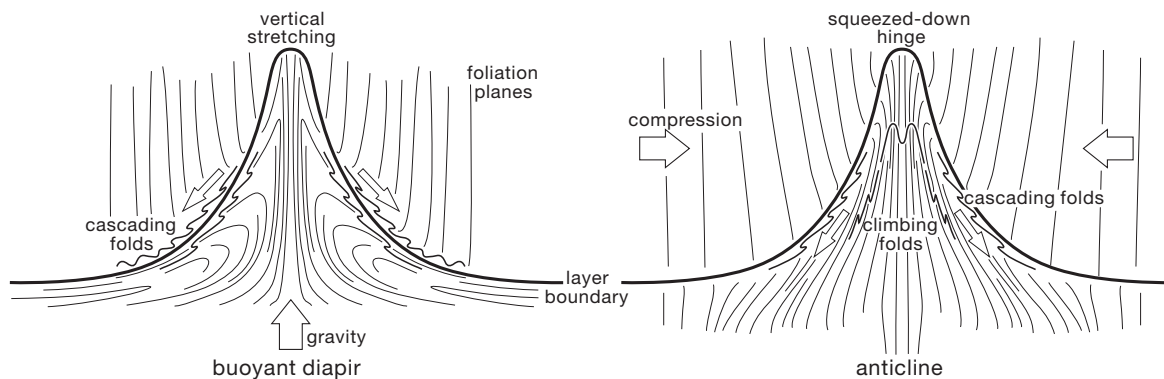


Figure 14. Structural characteristics of a diapir and a buckle-anticline submitted to instantaneous erosion as modeled in this work. This morphology refers to detachment diapirism and folding (Fig. 12).

opposite to expectations with a normal sense of shear at the interface. This is explained by the fact that the thin viscous channel largely controls deformation and, indeed, the strain pattern resembles that of viscous pipe flow. Only after extrusion of low-viscosity material, the finite strain pattern starts switching from normal to reverse sense of shear near the center of the dome, whereas in the diapir case the pattern remains relatively unchanged. We conclude that the present-day structural techniques applied for distinguishing diapiric domes and folds are ambiguous if detachment folding takes place and that domes displaying extensional structures do not necessarily reflect extension.

DISCUSSION

We have presented results for a two-layer system with simple Newtonian rheology, which is a fair approximation of the creep behavior of salt and sediments. However, rocks generally have a brittle rheology and/or a power-law rheology known to be depth-dependent through the strong temperature effect on the constitutive laws (e.g., Ranalli, 1995). In light of previous studies on folding and diapirism, we will first comment on the influence of power-law and brittle rheologies on our results. The main effect of power-law rheology on the folding instability is a marked increase in growth rates and a small decrease in dominant wavelength (e.g., Smith, 1977; Schmalholz et al., 2002; see also Equations 9 and 10). The same effect was also recognized for diapirs, around which the deformation aureole becomes smaller with increasing power law-exponent (Weinberg and Podladchikov, 1995).

Temperature dependency of viscosity may have an influence on the results presented here, which are, strictly spoken, only valid for quasi-adiabatic conditions. Thermal diffusion is known to be more effective if (1) growth rates of the instabilities are low and (2) the instability wavelength is small (e.g., Conrad and Molnar, 1997). Both conditions may exist in the thin-layer folding and thin-layer detachment modes (Fig. 5) and would slow the growth of domes. Since in crustal cases the viscosity differences are related to composition differences, the overall thermal effects are likely minor at initial stages. During evolved stages, however, cooling may stop domes from rising, an effect that will be more pronounced for short-wavelength structures. Nonlinear feedback mechanisms, such as those due to shear heating (e.g., Regenauer-Lieb and Yuen, 2003), may also modify the finite amplitude structures. Inspection of Figures 11 and 12 indicates that shear-heating may be most efficient for the detachment-folding mode, where it would potentially transform the two-layer system into a three layer system with a weak shear zone intercalated between the low-viscous layer and the highly-viscous overburden. The consequences of this intermediate zone on the geometry and dynamics of dome formation are currently unknown and should be addressed in future studies.

A brittle rheology has only minor effects on salt diapirism (Poliakov et al., 1996). Gerbault et al. (1999) also argued that

the brittle rheology has a relatively minor effect on lithospheric-scale folding. Zuber (1987) and Schmalholz et al. (2002) have considered the effect of a depth-dependent rheology. For this purpose, they redefined the thicknesses (H and H_m) of the layers during modeling; yet, the results remained similar to those obtained with depth-independent rheologies. Accordingly, one should expect that power-law and brittle rheologies will change the definitions of the two non-dimensional numbers B and B_{det} , but the main results of this paper, as first-order strain patterns and phase diagram, will not change significantly.

A point worth discussing again is the fact that natural folds are often non-periodic on a large scale, whereas they appear to be rather periodic on the outcrop scale. The simulations presented in this paper shed some light on this process by showing that instabilities starting from a larger initial perturbation grow faster. Recent work on viscoelastic folding pointed out that elasticity triggers more localized folding (e.g., Schmalholz and Podladchikov, 1999). Localization is also obtained if geometrical (with a non-dominant wavelength and finite amplitude) and/or rheological heterogeneities are present. It is obvious that a mountain chain like the Himalayas contained such heterogeneities at the onset of continental shortening (e.g., sutures, igneous intrusions, etc.). Therefore, large-scale folding, especially during continental collision, may naturally be localized. Folding of the oceanic lithosphere, on the other hand, is expected to be much more periodic, since the oceanic lithosphere is more homogeneous. It is thus logical that regular undulations in topography, gravity signal and Moho-depth observed in the Central Indian Basin over hundreds of kilometers (e.g., Zuber, 1987; Gerbault, 2000 and references therein) are periodic buckle folds. It is also evident that three-dimensional constraints linked to corner effects in original bends of continental boundaries (e.g., Brun and Burg, 1982) will force fold localization.

CONCLUSIONS

Simplified analytical calculations result in a phase diagram separating different modes of deformation as a function of two non-dimensional numbers: B and B_{det} . Five modes of deformation are important in non-extensional, crustal-scale doming, ranging from diapiric to folding modes. Numerical simulations further demonstrated that the evolved diapirs and folds are similar-looking chimney-like, rather isolated, domes, and erosion plays a key role in this isolation.

The strain distribution around domes allows the discrimination of folds versus diapirs only in the case where $B_{det} > 1$, implying that the low-viscosity lower layer is relatively thick. In the other cases, the use of asymmetric structures can erroneously point to a diapiric origin even if the dome has formed in compression only. If shortening continues after the core of the dome is eroded, important differences will be observed between diapirs and folds: the core of diapirs continues rising, whereas folds develop a core syncline reflecting downward movement in the center of the dome.

ACKNOWLEDGMENTS

We thank the Swiss National Fund, project number 21-61912.00, for financial support. This paper is part of Boris Kaus' Ph.D. thesis. We particularly thank Stefan Schmalholz for enlightening discussions and very constructive comments on a first draft of this manuscript. Dave Yuen and Peter Hudleston have provided very helpful reviews.

APPENDIX. PERTURBATION ANALYSIS

For geological processes, inertial terms can be ignored, and force equilibrium in a two-dimensional case, ignoring the effect of gravity, is given by:

$$\begin{aligned} \frac{\partial \sigma_{xx}}{\partial x} + \frac{\partial \sigma_{xz}}{\partial z} &= 0 \\ \frac{\partial \sigma_{xz}}{\partial x} + \frac{\partial \sigma_{zz}}{\partial z} &= 0 \end{aligned} \quad (\text{A1})$$

In addition, one assumes that material is incompressible:

$$\frac{\partial v_x}{\partial x} + \frac{\partial v_z}{\partial z} = 0 \quad (\text{A2})$$

Rheology is linearly viscous (with a constant viscosity μ inside each layer) and given by:

$$\begin{aligned} \sigma_{xx} &= -p + 2\mu \frac{\partial v_x}{\partial x} \\ \sigma_{zz} &= -p + 2\mu \frac{\partial v_z}{\partial z} \\ \sigma_{xz} &= -\mu \left(\frac{\partial v_x}{\partial z} + \frac{\partial v_z}{\partial x} \right) \end{aligned} \quad (\text{A3})$$

where p is pressure. Inserting Equations (A3) into the force-balance Equations (A1) gives:

$$\begin{aligned} -\frac{\partial p}{\partial x} + 2\mu \frac{\partial^2 v_x}{\partial x^2} + \mu \frac{\partial}{\partial z} \left(\frac{\partial v_x}{\partial z} + \frac{\partial v_z}{\partial x} \right) &= 0 \\ -\frac{\partial p}{\partial z} + 2\mu \frac{\partial^2 v_z}{\partial z^2} + \mu \frac{\partial}{\partial x} \left(\frac{\partial v_x}{\partial z} + \frac{\partial v_z}{\partial x} \right) &= 0 \end{aligned} \quad (\text{A4})$$

Pressure is eliminated by taking the derivative of the first equation versus z and subtracting the derivative of the second equation versus x :

$$2\mu \left(\frac{\partial^3 v_x}{\partial z \partial x^2} - \frac{\partial^3 v_z}{\partial x \partial z^2} \right) + \mu \left(\frac{\partial^2}{\partial z^2} - \frac{\partial^2}{\partial x^2} \right) \left(\frac{\partial v_x}{\partial z} + \frac{\partial v_z}{\partial x} \right) = 0 \quad (\text{A5})$$

We split the velocity in a sinusoidal perturbed part and a background part, due to the pure-shear shortening.

$$\begin{aligned} v_x &= \tilde{v}_x(z) \exp(I\omega x) - \dot{\epsilon}_{BG} x \\ v_z &= \tilde{v}_z(z) \exp(I\omega x) - \dot{\epsilon}_{BG} z \end{aligned} \quad (\text{A6})$$

where $I = \sqrt{-1}$ and $\dot{\epsilon}_{BG}$ is the background pure-shear strain rate assumed to be constant over the model. Inserting Equations (A6) into Equation (A5), using the incompressibility constraint (A3) and dividing by $\mu \exp(I\omega x) / \omega$ yields a fourth order ODE for $\tilde{v}_z(z)$:

$$\frac{\partial^4 \tilde{v}_z(z)}{\partial z^4} - 2\omega^2 \frac{\partial^2 \tilde{v}_z(z)}{\partial z^2} + \omega^2 \tilde{v}_z(z) = 0 \quad (\text{A7})$$

A general solution of Equation (A7) has the form:

$$\tilde{v}_z(z) = A e^{(\omega z)} + B z e^{(\omega z)} + C e^{(-\omega z)} + D z e^{(-\omega z)} \quad (\text{A8})$$

where A , B , C , and D are four constants. Having expressed $\tilde{v}_z(z)$, we can determine all other velocities, stresses, and the pressure from Equations (A2), (A3) and (A6), respectively.

The studied case is a two-layer system. Within each layer, Equation (A8) applies. Thus, there are eight unknown constants that need eight equations. Two of these equations apply at the no-slip lower boundary, lo , at $z = -H_m$ (Fig. 4):

$$\begin{aligned} \tilde{v}_z^{lo}(-H_m) &= 0 \\ \tilde{v}_x^{lo}(-H_m) &= 0 \end{aligned} \quad (\text{A9})$$

Two equations apply at the upper boundary, up , at $z = -H_m$, where an infinitely fast erosion boundary condition is set (Fig. 4):

$$\begin{aligned} \tilde{\sigma}_{zz}^{up}(H) &= 0 \\ \tilde{\sigma}_{xz}^{up}(H) &= 0 \end{aligned} \quad (\text{A10})$$

At the interface between the layers ($z = 0$), continuity of velocity is required. After making a first order Taylor expansion around ($z = 0$), the condition can be written:

$$\begin{aligned} \tilde{v}_x^{lo}(0) - \tilde{v}_x^{up}(0) &= 0 \\ \tilde{v}_z^{lo}(0) - \tilde{v}_z^{up}(0) &= 0 \end{aligned} \quad (\text{A11})$$

Stresses across the interface should also be continuous:

$$\begin{aligned} \tilde{\sigma}_{xz}^{lo}(0) - \tilde{\sigma}_{xz}^{up}(0) &= 4\dot{\epsilon}_{BG}(\mu_1 - \mu_2) \frac{\partial \eta}{\partial x} \\ \tilde{\sigma}_{zz}^{lo}(0) - \tilde{\sigma}_{zz}^{up}(0) &= (\rho_1 - \rho_2) g \eta \end{aligned} \quad (\text{A12})$$

where $\eta=A(t)\cos(\omega x)$ is the sinusoidally perturbed interface, and $A(t)$ is the perturbation amplitude, which grows exponentially with time. The growth on top of the background pure-shear thickening is given by:

$$A(t) = A_0 e^{(qt)} \quad (\text{A13})$$

where q is the growth rate of the interface.

Noting that: $\frac{\partial \eta}{\partial t} = \tilde{v}_z(0)$

one can derive that: $\eta = \frac{\tilde{v}_z(0)}{q}$

Substituting this relationship in Equations (A12) yields:

$$\begin{aligned} \tilde{\sigma}_{xz}^{lo}(0) - \tilde{\sigma}_{xz}^{up}(0) - 4\dot{\epsilon}_{BG}(\mu_1 - \mu_2)\omega \frac{\tilde{v}_z^{up}(0)}{q} &= 0 \\ \tilde{\sigma}_{zz}^{lo}(0) - \tilde{\sigma}_{zz}^{up}(0) - (\rho_1 - \rho_2)g \frac{\tilde{v}_z^{up}(0)}{q} &= 0 \end{aligned} \quad (\text{A14})$$

Equations (A9), (A10), (A11), and (A14) thus are eight equations for eight unknowns (A–F).

They can be written in matrix form:

$$\mathbf{AC}=\mathbf{R} \quad (\text{A15})$$

where \mathbf{A} is an 8 by 8 matrix containing coefficients in front of the unknowns (A–F), \mathbf{C} is an 8 by 1 vector containing the eight unknowns, and \mathbf{R} is an 8 by 1 vector, which is filled with zeros in the studied case.

The system (A15) has a nontrivial solution only if $\det(\mathbf{A}) = 0$. In practice, this tedious task is performed using the symbolic manipulation package MAPLE, but even in this case the analytical solutions are complicated. An alternative method was described in Smith (1977), who determines the growth rate q numerically by inserting a random value for q in \mathbf{A} and iterating until the $\det(\mathbf{A})$ is zero. This gives the growth rate for a given wave number and for given physical parameters. This task can be done using the linear algebra package MATLAB. By scanning ranges of ωs , the fastest growth rate is found. Analytical expressions of the maximum growth rate versus physical parameters were found by calculating growth rates for limiting cases (e.g., setting the background strain rate to zero gives pure diapiric modes). These analytical expressions were then compared to analytical expressions that were derived for simplified cases (e.g., the formula for dominant wavelength and growth rate for matrix folding was compared to an analyti-

cal solution that was derived for the case of folding if a layer rested on an infinite halfspace). Once expressions for growth rates are known for every deformation mode, the boundaries between deformation modes can be calculated by requiring that the growth rate of two adjacent phases are equal at the phase boundary.

REFERENCES CITED

- Abbassi, M.R., and Mancktelow, N.S., 1992, Single layer buckle folding in nonlinear materials.1. Experimental-study of fold development from an isolated initial perturbation: *Journal of Structural Geology*, v. 14, p. 85–104, doi: 10.1016/0191-8141(92)90147-O.
- Alavi, M., 1994, Tectonics of the Zagros orogenic belt of Iran: New data and interpretations: *Tectonophysics*, v. 229, p. 211–238, doi: 10.1016/0040-1951(94)90030-2.
- Arthaud, F., 1970, Etude tectonique et microtectonique comparée de deux domaines hercyniens: les nappes de la Montagne Noire (France) et l'anticlinorium de l'Iglesiente (Sardaigne): Montpellier, Université des Sciences et Techniques du Languedoc, série Géologie Structurale 1, 175 p.
- Biot, M.A., 1961, Theory of folding of stratified viscoelastic media and its implications in tectonics and orogenesis: *Geological Society of America Bulletin*, v. 72, p. 1595–1620.
- Biot, M.A., and Odé, H., 1965, Theory of gravity instability with variable overburden and compaction: *Geophysics*, v. 30, p. 213–227, doi: 10.1190/1.1439558.
- Brun, J.-P., 1983, L'origine des dômes gneissiques: Modèles et tests: *Bulletin de la Société Géologique de France*, v. 25, p. 219–228.
- Brun, J.-P., and Burg, J.-P., 1982, Combined thrusting and wrenching in the Ibero-Armorican arc: A corner effect during continental collision: *Earth and Planetary Science Letters*, v. 61, p. 319–332, doi: 10.1016/0012-821X(82)90063-2.
- Brun, J.-P., Gapais, D., and Le Theoff, B., 1981, The mantled gneiss domes of Kuopio (Finland): interfering diapirs: *Tectonophysics*, v. 74, p. 283–304, doi: 10.1016/0040-1951(81)90194-3.
- Brun, J.-P., and Pons, J., 1981, Strain patterns of pluton emplacement in a crust undergoing non-coaxial deformation, Sierra Morena, Southern Spain: *Journal of Structural Geology*, v. 3, p. 219–229, doi: 10.1016/0191-8141(81)90018-3.
- Burg, J.-P., Davy, P., Nievergelt, P., Oberli, F., Seward, D., Diao, Z., and Meier, M., 1997, Exhumation during crustal folding in the Namche-Barwa syntaxis: *Terra Nova*, v. 9, p. 53–56.
- Burg, J.-P., Nievergelt, P., Oberli, F., Seward, D., Davy, P., Maurin, J.-C., Diao, Z.Z., and Meier, M., 1998, The Namche Barwa syntaxis: Evidence for exhumation related to compressional crustal folding: *Journal of Asian Earth Sciences*, v. 16, p. 239–252, doi: 10.1016/S0743-9547(98)00002-6.
- Burg, J.-P., and Podladchikov, Y., 1999, Lithospheric scale folding: numerical modelling and application to the Himalayan syntaxes: *International Journal of Earth Sciences*, v. 88, p. 190–200, doi: 10.1007/S005310050259.
- Burg, J.-P., and Podladchikov, Y., 2000, From buckling to asymmetric folding of the continental lithosphere: Numerical modelling and application to the Himalayan syntaxes, in Khan, M.A., Treloar, P.J., Searle, M.P., and Jan, M.Q., eds., *Tectonics of the Western Himalayas and Karakoram*: London, Geological Society Special Publication 170, p. 219–236.
- Burov, E., Jaupart, C., and Guillou-Frottier, L., 2003, Ascent and emplacement of buoyant magma bodies in brittle-ductile upper crust: *Journal of Geophysical Research, Solid Earth*, v. 108, B4, no. 2177, doi: 10.1029/2002JB001904.
- Coney, P.J., and Harms, T.A., 1984, Cordilleran metamorphic core complexes: Cenozoic extensional relics of Mesozoic compression: *Geology*, v. 12, p. 550–554.
- Conrad, C.P., and Molnar, P., 1997, The growth of Rayleigh-Taylor-type instabilities in the lithosphere for various rheological and density structures: *Geophysical Journal International*, v. 129, p. 95–112.
- Currie, J.B., Patnode, H.W., and Trump, R.P., 1962, Development of folds in sedimentary strata: *Geological Society of America Bulletin*, v. 73, p. 655–674.

- Dixon, J.M., 1975, Finite strain and progressive deformation in models of diapiric structures: *Tectonophysics*, v. 28, p. 89–124, doi: 10.1016/0040-1951(75)90060-8.
- Dixon, J.M., 1987, Mantled gneiss domes, in Seyfert, C.K., ed., *The encyclopedia of structural geology and plate tectonics*: New York, Van Nostrand Reinhold Company, Inc., p. 398–412.
- England, P., and McKenzie, D.P., 1982, A thin viscous sheet model for continental deformation: *Geophysical Journal of the Royal Astronomical Society*, v. 70, p. 295–321.
- Eskola, P.E., 1949, The problem of mantled gneiss domes: *Quarterly Journal of the Geological Society of London*, v. 104, p. 461–476.
- Fletcher, R.C., 1972, Application of a mathematical model to the emplacement of mantled gneiss domes: *American Journal of Science*, v. 272, p. 197–216.
- Fletcher, R.C., 1977, Folding of a single viscous layer—Exact infinitesimal amplitude solution: *Tectonophysics*, v. 39, p. 593–606, doi: 10.1016/0040-1951(77)90155-X.
- Fletcher, R.C., 1991, 3-Dimensional folding of an embedded viscous layer in pure shear: *Journal of Structural Geology*, v. 13, p. 87–96, doi: 10.1016/0191-8141(91)90103-P.
- Fletcher, R.C., 1995, 3-Dimensional folding and necking of a power-law layer—Are folds cylindrical, and, if so, do we understand why: *Tectonophysics*, v. 247, p. 65–83, doi: 10.1016/0040-1951(95)00021-E.
- Gerbault, M., 2000, At what stress level is the central Indian Ocean lithosphere buckling?: *Earth and Planetary Science Letters*, v. 178, p. 165–181, doi: 10.1016/S0012-821X(00)00054-6.
- Gerbault, M., Burrov, E.B., Poliakov, A.N.B., and Daignières, M., 1999, Do faults trigger folding in the lithosphere?: *Geophysical Research Letters*, v. 26, p. 271–274, doi: 10.1029/1998GL900293.
- Goff, D., Wiltshko, D.V., and Fletcher, R.C., 1996, Decollement folding as a mechanism for thrust-ramp spacing: *Journal of Geophysical Research*, v. 101, p. 11341–11352, doi: 10.1029/96JB00172.
- Gzovsky, M.V., Grigoryev, A.S., Gushchenko, O.I., Mikhailova, A.V., Nikonov, A.A., and Osokina, D.N., 1973, Problems of the tectonophysical characteristics of stresses, deformations, fractures and deformation mechanisms of the Earth's crust: *Tectonophysics*, v. 18, p. 167–205, doi: 10.1016/0040-1951(73)90083-8.
- Hunt, G., Muhlhaus, H., Hobbs, B.E., and Ord, A., 1996, Localized folding of viscoelastic layers: *Geologische Rundschau*, v. 85, p. 58–64, doi: 10.1007/S005310050052.
- Ismail-Zadeh, A.T., Huppert, H.E., and Lister, J.R., 2002, Gravitational and buckling instabilities of a rheologically layered structure: Implications for salt diapirism: *Geophysical Journal International*, v. 148, p. 288–302, doi: 10.1046/J.1365-246X.2002.01612.X.
- Jackson, M.P.A., and Talbot, C.J., 1989, Anatomy of mushroom-shaped diapirs: *Journal of Structural Geology*, v. 11, p. 211–230, doi: 10.1016/0191-8141(89)90044-8.
- Kaus, B.J.P., 2004, Numerical modelling of geodynamical instabilities [Ph.D. thesis]: ETH Zurich.
- Kaus, B.J.P., and Podladchikov, Y.Y., 2001, Forward and reverse modeling of the three-dimensional viscous Rayleigh-Taylor instability: *Geophysical Research Letters*, v. 28, p. 1095–1098, doi: 10.1029/2000GL011789.
- Lavier, L.L., and Buck, W.R., 2002, Half graben versus large-offset low-angle normal fault: Importance of keeping cool during normal faulting: *Journal of Geophysical Research*, v. 107, no. B6, doi: 10.1029/2001JB000513.
- Mancktelow, N.S., 1999, Finite-element modeling of single-layer folding in elasto-viscous materials: The effect of initial perturbation geometry: *Journal of Structural Geology*, v. 21, p. 161–177, doi: 10.1016/S0191-8141(98)00102-3.
- Pitcher, W.S., 1979, The nature, ascent and emplacement of granitic magma: *Journal of the Geological Society of London*, v. 136, p. 627–662.
- Podladchikov, Y.Y., Talbot, C., and Poliakov, A.N.B., 1993, Numerical models of complex diapirs: *Tectonophysics*, v. 228, p. 189–198, doi: 10.1016/0040-1951(93)90340-P.
- Poliakov, A., Podladchikov, Y.Y., Dawson, E., and Talbot, C.J., 1996, Salt diapirism with simultaneous brittle faulting and viscous flow, in Alsop, I., Blundell, D., and Davison, I., eds., *Salt Tectonics*: London, Geological Society Special Publication 100, p. 291–302.
- Pons, J., Oudin, C., and Valero, J., 1992, Kinematics of large syn-orogenic intrusions: example of the Lower Proterozoic Saraya batholith (Eastern Senegal): *Geologische Rundschau*, v. 81, p. 473–486.
- Price, N.J., and Cosgrove, J.W., 1990, *Analysis of geological structures*: Cambridge, Cambridge University Press, 502 p.
- Ramberg, H., 1964, Selective buckling of composite layers with contrasted rheological properties, a theory for simultaneous formation of several orders of folds: *Tectonophysics*, v. 1, p. 307–341, doi: 10.1016/0040-1951(64)90020-4.
- Ramberg, H., 1971, Folding of laterally compressed multilayers in the field of gravity, II, Numerical examples: *Physics of the Earth and Planetary Interiors*, v. 4, p. 83–120, doi: 10.1016/0031-9201(71)90006-9.
- Ramberg, H., 1972, Theoretical models of density stratification and diapirism in the Earth: *Journal of Geophysical Research*, v. 77, p. 877–889.
- Ramberg, H., 1981, The role of gravity in orogenic belts, in McClay, K.R., and Price, N.J., eds., *Thrust and nappe tectonics*: London, Geological Society Special Publication 9, p. 125–140.
- Ramberg, H., and Stephansson, O., 1964, Compression of floating elastic and viscous plates affected by gravity: A basis for discussing crustal buckling: *Tectonophysics*, v. 1, p. 101–120, doi: 10.1016/0040-1951(64)90032-0.
- Ramsay, J.G., 1967, *Folding and fracturing of rocks*: New York, McGraw-Hill, 568 p.
- Ramsay, J.G., 1981, Tectonics of the Helvetic nappes, in McClay, K.R., and Price, N.J., eds., *Thrust and nappe tectonics*: London, Geological Society Special Publication 9, p. 293–309.
- Ramsay, J.G., 1989, Emplacement kinematics of a granite diapir: The Chindamora batholith, Zimbabwe: *Journal of Structural Geology*, v. 11, p. 191–209, doi: 10.1016/0191-8141(89)90043-6.
- Ranalli, G., 1995, *Rheology of the Earth*: London, Chapman and Hall, 413 p.
- Reddy, J.N., 1999, *Theory and analysis of elastic plates*: Philadelphia, Taylor and Francis, 540 p.
- Regenauer-Lieb, X., and Yuen, D., 2003, Modeling shear zones in geological and planetary sciences: Solid- and fluid-thermal-mechanical approaches: *Earth-Science Reviews*, v. 63, p. 295–349, doi: 10.1016/S0012-8252(03)00038-2.
- Schmalholz, S.M., Podladchikov, Y., and Burg, J.-P., 2002, Control of folding by gravity and matrix thickness: Implications for large-scale folding: *Journal of Geophysical Research*, v. 107, no. B1, ETG-1-1, doi: 10.1029/2001JB000355.
- Schmalholz, S.M., and Podladchikov, Y., 1999, Buckling versus folding: Importance of viscoelasticity: *Geophysical Research Letters*, v. 26, p. 2641–2644, doi: 10.1029/1999GL900412.
- Schmalholz, S.M., Podladchikov, Y.Y., and Schmid, D.W., 2001, A spectral/finite difference method for simulating large deformations of heterogeneous, viscoelastic materials: *Geophysical Journal International*, v. 145, p. 199–208.
- Schmeling, H., 1987, On the relation between initial conditions and late stages of the Rayleigh-Taylor instability: *Tectonophysics*, v. 133, p. 65–80, doi: 10.1016/0040-1951(87)90281-2.
- Smith, R.B., 1977, Formation of folds, boudinage, and mullions in non-Newtonian materials: *Geological Society of America Bulletin*, v. 88, p. 312–320.
- Smoluchowski, M., 1910, *Versuche ueber Faltungerscheinungen schwimmender elastischen Platten*: Akademie der Wissenschaften in Krakau, mathematisch-naturwissenschaftliche, Klasse, Reihe A, mathematische Wissenschaften, p. 727–734.
- Snowden, P.A., and Bickle, M.J., 1976, The Chindamora batholith: Diapiric intrusion or interference fold?: *Journal of the Geological Society of London*, v. 132, p. 131–137.
- Snowden, P.A., and Snowden, D.V., 1981, Petrochemistry of the late Archaean granites of the Chindamora batholith, Zimbabwe: *Precambrian Research*, v. 16, p. 103–129, doi: 10.1016/0301-9268(81)90007-3.
- Stipska, P., Schulmann, K., and Höck, V., 2000, Complex metamorphic zonation of the Thaya dome: Result of buckling and gravitational collapse of an imbricated nappe sequence, in Cosgrove, J.W., and Ameen, M.S., eds., *Forced folds and fractures*: London, Geological Society Special Publication 169, p. 197–211.
- Talbot, C.J., and Jackson, M.P.A., 1987, Internal kinematics of salt diapirs: *Bulletin of the American Association of Petroleum Geologists*, v. 71, p. 1068–1093.
- Teysseier, C., and Whitney, D.L., 2002, Gneiss domes and orogeny: *Geology*, v. 30, p. 1139–1142, doi: 10.1130/0091-7613(2002)0302.0.CO;2.
- Turcotte, D.L., and Schubert, G., 2002, *Geodynamics*: Cambridge, Cambridge University Press, 456 p.

- Vigneresse, J.-L., and Clemens, J.D., 2000, Granitic magma ascent and emplacement: Neither diapirism nor neutral buoyancy, *in* Vendeville, B., Mart, Y., and Vigneresse, J.-L., eds., *Salt, shale and igneous diapirs in and around Europe*: London, Geological Society Special Publication 174, p. 1–19.
- Weinberg, R.F., and Podladchikov, Y., 1995, The rise of solid-state diapirs: *Journal of Structural Geology*, v. 17, p. 1183–1195, doi: 10.1016/0191-8141(95)00004-W.
- Whitehead, J.A., 1988, Fluid models of geological hotspots: *Annual Review of Fluid Mechanics*, v. 20, p. 61–87, doi: 10.1146/ANNUREV.FL.20.010188.000425.
- Woidt, W.D., 1978, Finite element calculations applied to salt dome analysis: *Tectonophysics*, v. 50, p. 369–386, doi: 10.1016/0040-1951(78)90143-9.
- Zeitler, P.K., Chamberlain, C.P., and Smith, H.A., 1993, Synchronous anatexis, metamorphism, and rapid denudation at Nanga Parbat (Pakistan Himalaya): *Geology*, v. 21, p. 347–350, doi: 10.1130/0091-7613(1993)0212.3.CO;2.
- Zhang, Y., Mancktelow, N.S., Hobbs, B.E., Ord, A., and Muhlhaus, H.B., 2000, Numerical modelling of single-layer folding: clarification of an issue regarding the possible effect of computer codes and the influence of initial irregularities: *Journal of Structural Geology*, v. 22, no. 10, p. 1511–1522, doi: 10.1016/S0191-8141(00)00063-8.
- Zuber, M.T., 1987, Compression of oceanic lithosphere: An analysis of intra-plate deformation in the Central Indian basin: *Journal of Geophysical Research*, v. 92, p. 4817–4825.
- Zwart, H.J., 1967, The duality of orogenic belts: *Geologie en Mijnbouw*, v. 46, p. 283–309.

MANUSCRIPT ACCEPTED BY THE SOCIETY APRIL 8, 2004